

INTEGRATED MASTER'S IN ENVIRONMENTAL ENGINEERING 2019/2020

**TRANSPORT LIMITATIONS IN POLYMER ELECTROLYTE MEMBRANE
FUEL CELL ELECTRODES**

LUIZ CARLOS REIS AJUS

Dissertation submitted for the degree of

MASTER ON ENVIRONMENTAL ENGINEERING

President of the jury:

Cidália Maria de Sousa Botelho

Assistant Professor of the Chemical Engineering department of the Faculty of Engineering of the
University of Porto

Supervisor at the University:

Adélio Miguel Magalhães Mendes

Full Professor in the Chemical Engineering department of the Faculty of Engineering of the
University of Porto

Supervisor at Foreigner University (or company):

Jens Mitzel

Research assistant at the German Aerospace Center (DLR) in Stuttgart

October and 2020

Acknowledgment

I would like to thank all those who have collaborated directly or indirectly in the completion of this study.

First, I would like to thank my supervisors, Dr. Jens Mitzel and Prof. Adélio Mendes, who guided, referred, advised, and reassured me throughout the development of this project. I also gratefully acknowledge Siegfried Graf, Wolfgang Schröder, and Thomas Lorscheider for the installation of the used test equipment and the development of the WinCC applications for test bench control as well as data acquisition and visualization. Without them, we certainly would not have been able to complete this work.

Let's also not forget to thank my colleagues at DLR, Qian Zhang, Krishan Talukdar, and Manigah Nazari, who were very supportive during times of doubt and stress.

Finally, he wanted to thank his family and friends, Isabella Tomasi, João Paulo Ortigão, Túlio Mafra, João Pedro Tavares, Leonardo Silva, and Pedro Nogueira for supporting him, encouraging him, and having believed in his abilities not only during this work but also during all the duration of my studies.

Prof. Adélio Mendes, supervisor of this dissertation, are integrated members of LEPABE - Laboratory of Process Engineering, Environment, Biotechnology and Energy, financed by: Base Financing - UIDB / 00511/2020 of the Research Unit - Laboratory of Process Engineering, Environment, Biotechnology and Energy - LEPABE - financed by national funds through FCT / MCTES (PIDDAC).



Abstract

Polymer electrolyte membrane fuel cell (PEMFC) can convert the chemical energy through electrochemical reaction to electrical energy with high efficiency. This technology enables powering electric automotive, portable, and stationary devices without producing any harmful emissions to the environment. There has been an effort to adapt it to the high-power density and durability standards of the automotive sector while keeping it commercially marketable and competitive.

One step into making it cost-efficient is reducing the platinum loading of the membrane electrode assembly (MEA) used on the energy conversion. Moreover, the cell's performance at high currents densities (HCD) suffers from significant mass transport limitations that shorten the PEMFC's lifetime and limits its maximum power output, making it unfit for automotive purposes. Amid the recent progress achieved, the requirement of operating at HCD to fit the spatial limitations of a conventional automobile is the main shortcoming of this technology.

The study herein tested the performance of a commercial MEA with 25 cm² produced by Gore Fuel Cell Technologies with the operating parameters validated by the automotive sector for PEMFC usage while assessing the impact of oxygen concentration (10 %, 15 %, 20.95 %, and 30 %) and cathodic stoichiometry (1.6, 1.8, 2.0, and 2.2) changes in the reactant feed stream. Mass transport resistance always affected the performance at 0.8 A·cm² when coupling 10 % oxygen and cathode's stoichiometry of 1.6. At the low current density (LCD) region, switching to 30 % oxygen concentration instead of 10 % oxygen concentration only granted a 4 % increase in the power output. At high current density HCD (2.0 A·cm²), this difference grew to 22 % (now comparing 15 % oxygen concentration to 30 % due to some limitations in the installation).

Electrochemical impedance spectroscopy (EIS) was employed to diagnose the impact the chosen variables had on the mass transport limitations of the cell. An equivalent electric circuit (EEC) was selected to replicate the cell's electrical behavior. The mathematical output of this fitting allowed the quantification of the primary resistances contributing to the performance loss. The mass transport was the most significant resistance at HCD and ranged from about 0.1 to 0.3 Ω·cm², and the lowest assessed loss at LCD was going from about 0.01 to 0.03 Ω·cm². The EIS was also useful to identify water management issues at 0.5 A·cm² due to the configuration of the flow field multi-serpentine pattern. This issue was not detected during this thesis when using a flow field with a single-serpentine gas channel (GC). Consequently, the characterization setup could be significantly improved for further research.

Keywords (theme): Polymer Electrolyte Fuel Cell, Mass Transport, Electrochemical Impedance Spectroscopy, Cathode.

Resumo

As pilhas de combustível com eletrólito de membrana (*PEMFC*) conseguem converter energia química em energia elétrica de elevada eficiência através de uma reacção electroquímica. Esta tecnologia permite alimentar automóveis eléctricos, bem como aparelhos móveis e fixos sem produzir qualquer emissão prejudicial para o ambiente. Tem sido feito um enorme esforço de adaptação desta tecnologia aos padrões e requisitos de elevada potência e durabilidade do sector automóvel ao mesmo tempo que se procura que seja comercialmente acessível e competitivo.

Uma forma de o tornar economicamente mais acessível é reduzir a carga de platina do conjunto de eletrodo de membrana (*MEA*) usada na conversão de energia. Além disso, o desempenho da célula em correntes de alta densidade (*HCD*) apresenta perdas significativas de transferência de massa que reduzem o tempo de vida da *PEMFC* e a sua máxima potência produzida, tornando-a desajustada para a indústria automóvel. Com os últimos progressos ocorridos, a necessidade de funcionar em correntes de alta densidade de modo a cumprir as limitações de espaço de um automóvel convencional é a principal lacuna desta tecnologia.


O estudo aqui apresentado testou a performance de uma *MEA* comercial com 25 cm², produzida pela empresa *Gore Fuel Cell Technologies*, com os parâmetros operacionais validados pelo sector automóvel para a utilização de *PEMFC*, avaliando o impacto da alteração da concentração de oxigénio (10 %, 15 %, 20.95 %, e 30 %) e a mudança de estequiometria catódica (1,6, 1,8, 2,0, e 2,2) no fluxo de alimentação do reagente. A resistência de transferência de massa afectava sempre o desempenho a 0,8 A·cm² quando se juntava os 10 % de oxigénio com estequiometria de cátodo de 1,6. Na zona de corrente de baixa densidade (*LCD*), substituindo por uma concentração de 30 % de oxigénio ao invés dos 10 % testados anteriormente, deparamo-nos com um aumento de apenas 4 % da potência aferida. Em corrente de alta densidade (2.0 A·cm²), esta diferença aumentou cerca de 22 % (agora comparando uma concentração de oxigénio de 15 % com 30 % devido a algumas limitações na sua instalação).

Foi utilizada espectroscopia de impedância electroquímica (*EIS*) para avaliar o impacto que as variáveis escolhidas tinham nas limitações de transferência de massa da célula. Foi seleccionado um circuito eléctrico equivalente (*EEC*) para reproduzir e replicar o comportamento eléctrico da célula. O resultado matemático deste trabalho permitiu a quantificação das resistências primárias que contribuem para a redução da sua performance. A transferência de massa foi a principal resistência a correntes de alta densidade com variações aproximadamente entre 0,1 e 0,3 Ω·cm² e, simultaneamente, a perda menos expressiva em corrente de baixa densidade, desta feita ficando compreendida entre ~0,01 e 0,03 Ω·cm².

Consequentemente, a configuração da caracterização pode ser melhorada significativamente com mais pesquisa.

Declaration

I hereby declare, under the word of honor, that this work is original and that all non-original contributions are indicated, and due reference is given to the author and source



October 26, 2020

Index

1	Introduction.....	1
1.1	Framing and presentation of the work	1
1.2	Presentation of the company.....	4
1.3	Contribution of the author to the work	4
1.4	Organization of the thesis.....	5
2	Context and state of the art	7
3	Materials and methods.....	11
3.1	PEMFC	11
3.2	Performance test.....	12
3.3	Mass transport diagnosis.....	13
4	Results and discussion	15
4.1	Polarization curves	15
4.2	EIS measurement.....	22
4.3	EIS fitting	34
5	Conclusion.....	41
6	Assessment of the work done	43
6.1	Objectives Achieved.....	43
6.2	Final Assessment	43
7	References	45

List of Figures

Figure 1 Structure and principal components of PEMFC (adapted from (Biswas et al., 2020).2

Figure 2 typical i-V plot of fuel cell performance including three regions dominated by different losses (adapted from (Biswas et al., 2020)3

Figure 3 Single PEMFC structure: Anode (A), Gas channel (B), Cathode (C), MEA (D) and GDL (E)8

Figure 4 cellFIX device attached to the test station and with the PEMFC in place 11

Figure 5 MEA (A.1) and both GDLs (A.2) cut from the commercial main piece. Assembled cell being maintained (B). 12

Figure 6 external ZS electronic load used on potentiostic mode 12

Figure 7 Display of the Zahner software to enable/disable parameters to customize the fitting (A). Results of the fitting (B) 14

Figure 8 Impact of oxygen concentration change on the polarization curve plots grouped by stoichiometry (A) 1.6, (B) 1.8, (C) 2.0, (D) 2.2 16

Figure 9 Closer look on the impact of oxygen concentration change for the polarization curve with stoichiometry of 1.6 17

Figure 10 impact of stoichiometry change on the polarization curve plots grouped by oxygen concentration (A) 10 %, (B) 15 %, (C) 20.95 %, (D) 30 %..... 18

Figure 11 Zoom in of Figure 10 B - impact of stoichiometric change for the polarization curve with 15 % oxygen concentration. 18

Figure 12 Comparison of the polarization curves and its respective power curve for the oxygen stoichiometry of interest (1.6) grouped by the different oxygen concentrations used 20

Figure 13 Instability of the flow meter for volumes under its precision range (roughly 10 % of its maximum value) 21

Figure 14 Test bench display while running the polarization curves with 1.5 bar and 1.2 A·cm⁻² (A) and 15 A (B). Sudden drops in performance were noticed and corrupted the data for making any precise analysis..... 22

Figure 15 EIS plots for the stoichiometry of 1.6 (A) with 10 % oxygen, (B) with 15 % oxygen, (C) with 20.95 % oxygen, and (D) with 30 % oxygen 23

Figure 16 EIS plots for the stoichiometry of 1.6 measured with 0.625 A (A), 12.5 A (B), 25 A (C) and 35 A (D)..... 24

Figure 17 EIS plots for 0.625 A (0.025 A·cm²) and a perturbation of 50mA under the oxygen stoichiometry of 1.6 (A), 1.8 (B), 2.0 (C), and 2.2 (D) 25

Figure 18 impact of the oxygen concentration on the EIS plots at 12.5 A ($0.5 \text{ A}\cdot\text{cm}^2$) for the oxygen stoichiometry of 1.6 (A), 1.8 (B), 2.0 (C), and 2.2 (D) 26

Figure 19 Impact of the oxygen stoichiometry change in the EIS plots measured at 12.5 A ($0.5 \text{ A}\cdot\text{cm}^2$) with (A) 10 % oxygen, (B) 15 % oxygen, (C) 20.95 % oxygen, and (D) 30 % oxygen in the reactant stream 27

Figure 20 Closer look in the EIS plots at 12.5 A ($0.5 \text{ A}\cdot\text{cm}^2$) with different operating pressures and oxygen stoichiometry of (A) 1.6, (B) 1.8, (C) 2.0, and (D) 2.2 28

Figure 21 Flow field of the ID fast fuel cell (A). The blue arrows indicate the path followed from inlet to outlet. Single-serpentine flow field design tested (B)..... 29

Figure 22 - Impact of the flow field structure on the EIS plots at 12.5 A ($0.5 \text{ A}\cdot\text{cm}^2$) at 2.2/2.0 bar with the stoichiometry of (A) 1.6, (B) 1.8, (C) 2.0, and (D) 2.2 30

Figure 23 Impact of the oxygen concentration on the EIS plots at 25 A ($1 \text{ A}\cdot\text{cm}^2$) with the oxygen stoichiometry of (A) 1.6, (B) 1.8, (C) 2.0, and (D) 2.2 31

Figure 24 Closer look in the EIS plots at 25 A ($1.0 \text{ A}\cdot\text{cm}^2$) with different operating pressures and oxygen stoichiometry of (A) 1.6, (B) 1.8, (C) 2.0, and (D) 2.2 32

Figure 25 Impact of the oxygen concentration on the EIS plots at 35 A ($1.4 \text{ A}\cdot\text{cm}^2$) with the oxygen stoichiometry of (A) 1.6, (B) 1.8, (C) 2.0, and (D) 2.2 33

Figure 26 Closer look in the EIS plots at 35 A ($1.4 \text{ A}\cdot\text{cm}^2$) with different operating pressures and oxygen stoichiometry of (A) 1.6, (B) 1.8, (C) 2.0, and (D) 2.2 34

Figure 27 Zahner's display for modeling the electric circuit. The chose one has one inductive element (1), resistive element (2), and two parallel sets (RCPE) (3, 4, 5, and 6) 34

Figure 28 Comparison of the EIS spectrum (dotted line) and the model's electrical behavior plot (solid line) 35

Figure 29 Z-Hit correlation done by the Zahner software to enable interpolation of the data in the fitting procedure 35

Figure 30 Fitting results for the EIS measurement of 0.625 A ($0.025 \text{ A}\cdot\text{cm}^2$) 36

Figure 31 Fitting results for the EIS measurement of 12.5 A ($0.5 \text{ A}\cdot\text{cm}^2$) 37

Figure 32 Fitting results for the EIS measurement of 25 A ($1.0 \text{ A}\cdot\text{cm}^2$)..... 38

Figure 33 - Fitting results for the EIS measurement of 35 A ($1.4 \text{ A}\cdot\text{cm}^2$) 39

...

List of Tables

Table 1 Parameters applied to the PEMFC operation while running the tests..... 13

Table 2 Voltage and power data (oxygen stoichiometry of 1.6)..... 21

...

Notation and glossary

I	current	A
$\text{Im}(Z)$	imaginary part of the impedance spectrum	$\Omega \cdot \text{cm}^2$
j	current density	$\text{A} \cdot \text{cm}^{-2}$
j_0	exchange current density	$\text{A} \cdot \text{cm}^{-2}$
P	power density	$\text{W} \cdot \text{cm}^{-2}$
R_{el}	ohmic or electrolyte resistance	$\Omega \cdot \text{cm}^2$
R_{diff}	mass transport resistance	$\Omega \cdot \text{cm}^2$
R_{pol}	polarization or charge transfer resistance	$\Omega \cdot \text{cm}^2$
$\text{Re}(Z)$	real part of the impedance spectrum	$\Omega \cdot \text{cm}^2$
U	voltage	V
E°	thermodynamic standard electrode potential	V

Greek Letters

λ	stoichiometry
-----------	---------------

List of Acronyms

CL	Catalyst layer
ECSA	Diffusion media
EEC	Equivalent electric circuit
EIS	Electrochemical impedance spectroscopy
GC	Gas channel
GDL	Gas diffusion layer
GHG	Greenhouse gases
HCD	High current density
HOR	Hydrogen oxidation reaction
LCD	Low current density
MEA	Membrane electrode assembly
ORR	Oxygen reduction reaction
PEM	Polymer electrolyte membrane
PEMFC	Polymer electrolyte membrane fuel cell
PGM	Platinum group metals
RCPE	Randles circuit
RH	Relative humidity

1 Introduction

1.1 Framing and presentation of the work

The transition from fossil to renewable fuels as the primary source of power supply for most sectors of our society is the path to overcome the climate change challenges and achieve the commitments taken under the Paris Agreement of 2016 within the UNFCC (United Nations Framework Convention on Climate Change) and UN resolution 70/1 (Wood *et al.*, 2019).

The combustion process of the hydrocarbon matrix to produce power is responsible for Greenhouse Gases (GHG) emissions that contribute directly to Global Warming. Moreover, its products and sub-products (NO_x , SO_x , and particulate matter) are held accountable for most of the actual respiratory diseases, air pollution, acidification of soils, and forest damage. Since 1980, the Netherlands established policies aiming for the limitation of its emissions. It is estimated to have spared more than 66 000 lives and to have avoided more than 70 billion euros on health expenses (Velders *et al.*, 2020).

Fossil fuels play a significant role in our economy. Answerable for an industry that holds thousands of jobs and is the principal asset of a limited group of countries. Its influence for more than centuries in geopolitics has often led to warfare, shaping power relations between the nation's fuels. It's practically unnoticed decrease in the global energy share, despite the worldly awareness of its responsibility on climate change effects (Wood *et al.*, 2019). Fortunately, the recent growth in the renewable fuel technology market sheds light on a possible change.

In recent years we have experienced the increase of solar and wind as competitors of the traditional carbon-based matrix. Its storage capacity limits the growing share of these renewable energy sources as the energy supply by solar and wind is unstable. Efficient energy converters are required to sustain this increase. Thus, the concept of gravimetric power density or specific power is crucial when comparing the available technologies. They translate the total amount of power supplied per unit of mass. In other words, the bigger the device producing energy, the bigger the power it can deliver. Polymer electrolyte membrane fuel cell (PEMFC) outperforms all the other existent technologies on that matter.

PEMFC is an energy converter that provides electrical and thermal power continuously while being fed. It takes the chemical power within the fuel and converts it to electrical power with high efficiency by electrochemical reactions. Thermal energy is generated as a side product. Most fuel cells run on hydrogen and atmospheric air as the primary source of reactants, producing water and heat. It's not only interesting for reducing the emission of greenhouse

gases but as its primary fuel is hydrogen (H_2), it can be produced on the spot using renewable energy sources and electrolysis.

The basic structure of a PEMFC can be split into three main components: The anodic side, the cathodic side, and the polymer electrolyte membrane (PEM) in between (Figure 1). The anode side is where the hydrogen is delivered through the diffusion medium (DM) or gas diffusion layer (GDL) that enables the contact with an electrode in the catalyst layer (CL) to spark the hydrogen oxidation reaction (HOR). The PEM to electrically shield one from another, forcing the electrons to take a longer path, producing the desired electric current. It is made of a polymer material that provides mobility to the protons (H^+) (HOR products) to flow to the cathode side. On the cathode side, in a similar fashion as the anode side but fed with atmospheric air, protons and the electrons recombine them to produce water in the oxygen reduction reaction (ORR).

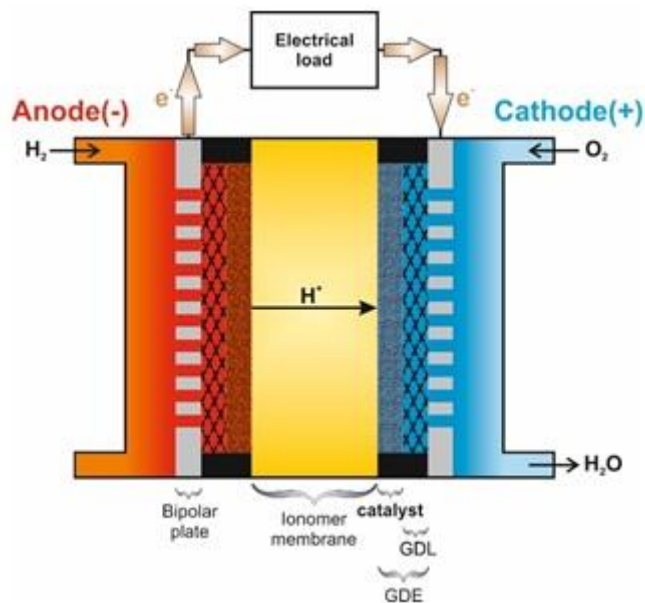


Figure 1 Structure and principal components of PEMFC (adapted from (Biswas *et al.*, 2020).

PEMFC's performance is related to the total surface area available for the conversion of chemical into electrical energy, the so-called electrochemical active surface area (ECSA). The heterogeneity of electrochemical reactions requires interfacial contact to take place. Thus, the intimate intersection of gas (fuel), an electrically conductive electrode, and an ion-conductive electrolyte are pivotal to its accomplishment (O'hayre *et al.*, 2016). Usually referred to as the triple-phase zone, the quantity of those active sites increases the probability of completion of electrochemical reactions. The homogenous distribution of reactants and ECSA is demanded to maximize overall performance and avoid lifetime shortening of its components (Daniel R. Baker *et al.*, 2009).

Thermodynamics dictates some penalties that reduce the useful potential, compromising performance. The three major causes: Activation losses due to the electrochemical reaction

itself and are noticeable at very low current densities (region I in Figure 2); Ohmic losses, which are mainly linked to the ionic and protonic transport between its components, pronounced at middle range current density (region II in Figure 2); and the most critical of them, concentration losses, associated with mass transport resistance and occurs on desirable higher current density operation (region III in Figure 2). Plotting i - V and power density curves for a fuel cell allow us to know how it will perform under different working conditions. Those significant losses can be easily distinguished when we look at Figure 2. Each loss ensures a specific drop on the polarization curve from which mass transport causes the most severe one (O'hayre *et al.*, 2016).

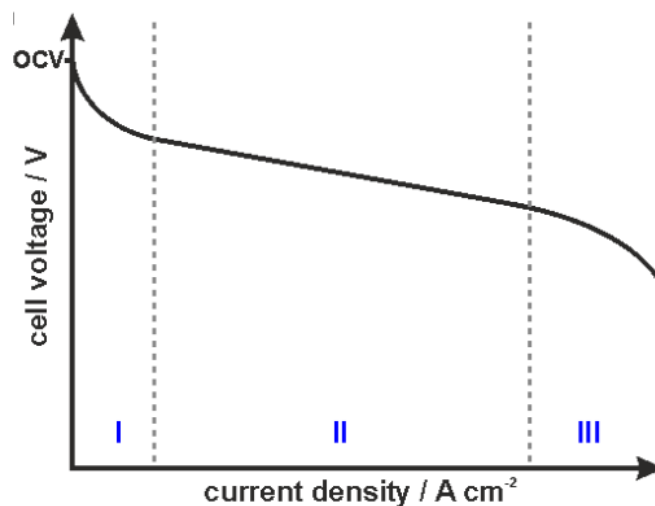


Figure 2 typical i - V plot of fuel cell performance including three regions dominated by different losses (adapted from (Biswas *et al.*, 2020))

Mass transport losses can be fractioned into different resistances that restrict oxygen diffusion inside the cell. Reasons for that vary locally due to water formation that is not removed during cell operation, therefore, creating a more significant barrier for gas diffusion by flooding. PEMFC operation under dry conditions cannot reach optimal results because it affects the ionic transport of protons by the membrane (O'hayre *et al.*, 2016). Water management and humidity control are required. In addition to this, the ionomer may clog the catalyst (Kongkanand *et al.*, 2016) or become inactive due to carbon poisoning (Reshетенko *et al.*, 2014), thus, reducing active reaction sites.

As far as fuel cell performance is concerned, the reaction kinetics is core to its improvement. Electrochemical reactions do occur spontaneously if some conditional restraints are met. PEMFC's optimal working conditions are around 80-100 °C and 1-3 bar (Hogarth *et al.*, 2006). Compared to other fuel cell variations, its lower working temperature negatively influences reaction kinetics. The addition of catalysts and the design of a highly porous nanostructured electrode counterbalance that. However, Platinum Group Metals (PGM) are the best catalysts

yet tested and one of the rarest elements on Earth. The PGM loading challenges its mass production as it increases its retail price (Kongkanand *et al.*, 2016).

The overall reaction that governs the electricity production in PEMFCs is limited by the rate of completion of its sluggish step. ORR has more intermediary half-reactions and a more significant activation loss when compared to HOR. Although feeding the cathode with atmospheric air (about 21 % oxygen in mainly nitrogen) is cost-efficient, oxygen diffusion into nitrogen and reduced partial pressure have its price. This power loss compromises the available power once it is upper restricted thermodynamically (O'hayre *et al.*, 2016). Therefore, being able to diminish those losses parallel to current density increase provides us a more efficient technology with more usable power.

Understanding the transport limitations on membrane polymer electrodes allows us to define why and how they happen. Mastering this obstacle can grant high-performance fuel cells under high current densities, obtaining cost-efficient green technology with zero harmful emissions. The scope of this study is to precisely determinate and comprehend the main factors accountable for the sharp drop due to mass transport losses and how to mitigate them. The presented work provides working material for the improvement of PEMFC applicability in our daily lives as it relies on the operation under high current densities to fulfill both our power and spatial demands (Nonoyama *et al.*, 2011).

1.2 Presentation of the company

The DLR-Institute of Technical Thermodynamics is active in the fields of renewable energy research and technology development for efficient and low emission energy conversion and utilization. The division Electrochemical Energy Technology has long-term experience in fuel cells and production technologies, e.g., plasma technology, rolling, and cold dry spraying techniques. The division also has extensive experience in the characterization of components of electrochemical energy converters with electrochemical and physical methods as well as in the diagnostics of fuel cells. Around 60 persons work in the division, 20 persons in the field of PEMFC research and development. Besides, numerous people work in the analytic of components for electrochemical systems.

1.3 Contribution of the author to the work

During his work as a student assistant in the ECE group of the electrochemical department of the Institute of Thermodynamics at DLR, he was able to contribute with the:

- Commissioning, support, and further development of fuel cell test stands
- Improvement of the script flow of the test stands
- Optimization of the structure for fuel cell characterization

- In-situ and ex-situ characterization of fuel cell components
- Systematic investigation of the influences of the fuel cell operating parameters to investigate their impact on transport processes.
- Planning and conducting of test campaigns regarding mass transport limitations, data analysis, impedance data fitting and result interpretation.

1.4 Organization of the thesis

The thesis's structure has seven chapters. The first two, Introduction and Context and State of the art, aim at giving a broader prospect of the theme and demonstrate the relevance of the present study to the actual scenario of the subject. The next chapter, Materials and Methods, give an overview of the methodology used and the equipment employed to reproduce to work herein. Followed by Results and Discussion, this section reveals the data obtained and the assumptions raised by them. The Conclusion sums up all the previous chapters and validates the work done. The sixth chapter, Assessment of the work done, applies criticism and ideas for future topics. The thesis ends with the Reference chapter, where is disposed all the accessed literature and also acknowledges the contributions of other writers from whom the author may have borrowed some words and ideas.

2 Context and state of the art

Polymer electrolyte membrane fuel cells (PEMFCs) efficiently convert the chemical energy through electrochemical reactions to electrical energy (Handbook, 2004; Larminie *et al.*, 2003; O'hayre *et al.*, 2016). Those devices can deliver high power densities and, when fueled by green hydrogen, provide emission-free electricity for stationary, portable, and automotive use (!!! INVALID CITATION !!! (A. Kongkanand *et al.*, 2016; Mitzel *et al.*, 2020)). The interest in this technology has been boosted by the actual trend in the automotive sector of finding alternatives for fossil fuel dependency and environmental awareness (Fukuyama *et al.*, 2014). The chemical energy of the fuel is converted into electrical power catalyzed by platinum, which belongs to the platinum-group metals or PGM. It represents the significant hold back for the acceptancy of its commercialization on an industrial scale. Not only overcoming the challenge of cost reduction coupled with power density compactness, it must meet the safety standards and durability requirements to be able to enter the competition with ICE (internal combustion engines) vehicles (Fukuyama *et al.*, 2014; Kongkanand *et al.*, 2019; Kongkanand *et al.*, 2016).

PEMFCs are usually grouped in series, commonly referred to as stacks, to meet the required power output (Larminie *et al.*, 2003). Although, one must look to its configuration to understand and improve the concept behind its operation. The typical PEM fuel cell can be split into three major components: the anodic side, the cathodic side, and the MEA (membrane electrode assembly) (Handbook, 2004; O'hayre *et al.*, 2016). It can also be fractioned into seven layers: Two gas channels (GCs) being one in the anode and the other in the cathode, two gas diffusion layers (GDLs), or porous diffusion media overlaying each GC, two catalyst layers (CLs) with one electrolyte membrane in between them. Figure 3 depicts all the cells tested herein to illustrate all the pre-mentioned compartments. The characterization of the fuel cell structure leads the path to reduce its negative impact on the overall performance. Engineers have tailored bipolar plates that enable sequentially connecting the cathode and the anode of the individual cells with minor interference on the output power (Larminie *et al.*, 2003). Nowadays, the focus of concern is the reduction of PGM catalysts of the CL while keeping high efficiency of conversion of the chemical energy of the fuel (Fukuyama *et al.*, 2014; Greszler *et al.*, 2012; Kongkanand *et al.*, 2019; Kongkanand *et al.*, 2016).

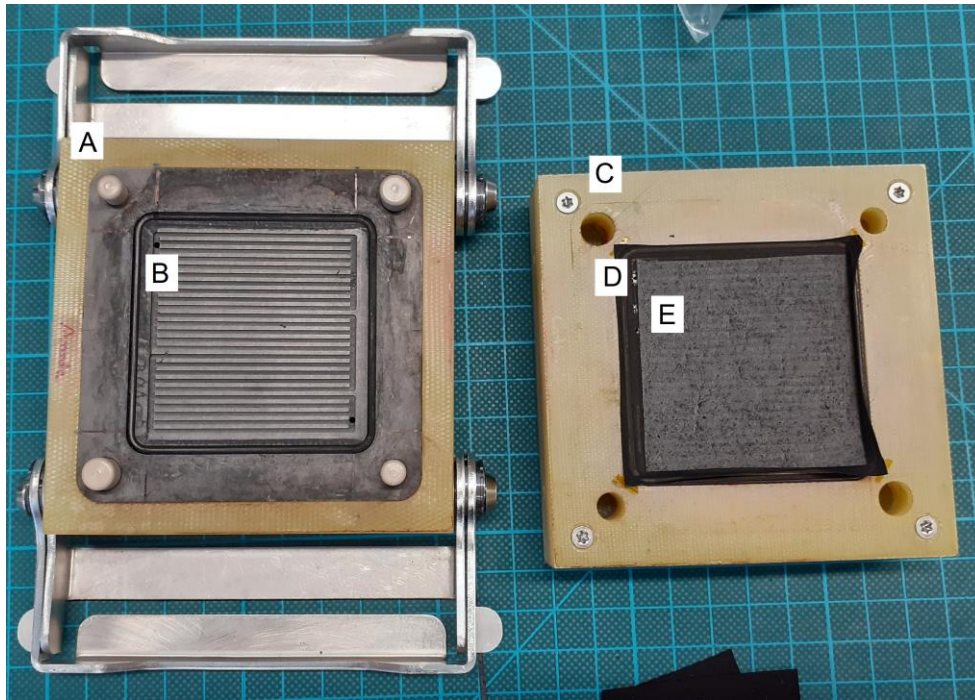
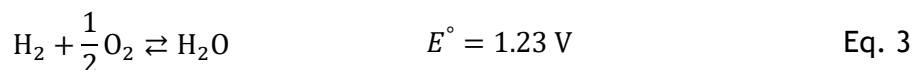
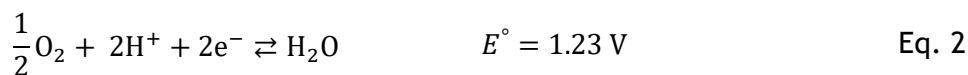
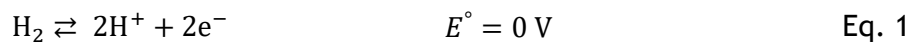


Figure 3 Single PEMFC structure: Anode (A), Gas channel (B), Cathode (C), MEA (D) and GDL (E)

The PEMFC is fueled with hydrogen in the anode side and fed with a reactant stream, usually oxygen, in the cathode. Inside the anode, the potential difference drawn from the cell oxidizes the hydrogens molecules, which split into H^+ ions (protons) and electrons (Eq. 1). The electrolyte membrane enables the passage of the ions. Still, it blocks the electrons, forcing them to take a longer path and thus providing current to the external system connected to the fuel cell. Simultaneously, inside the cathode, the oxygen is recombined with the H^+ ion and the electron coming from the anode to form water and heat (Eq. 2). Those two half-reactions sum up to create the primary electrochemical reaction (Eq. 3) that governs the energy conversion from chemical energy to electrical energy (Kabza, 2015).



The E° is the thermodynamic standard electrode potential. Although those 1.23 V are not available to be converted into electricity, this reflects only the amount of energy this reaction produces - the Gibbs free energy of the system. The actual power output that can be harvested from a PEMFC is affected by different types of resistances intrinsic to the use of this technology. Looking from a macro point of view, they can be grouped into three distinct groups: Activation losses, ohmic losses, and mass transport losses. The first two can be easily tackled by material

choice and operational parameters, while the last one is still not well understood. Those resistances are responsible for consuming the available potential and thus impacting the effectiveness of the process. Understanding them and learning how to minimize their relevance during cell operation is what yields the adoption of this technology from a commercial standpoint.

Mass transport losses have been the focus of intensive search. These losses mainly appear on the cathode and can be understood as the losses caused by limited transport of oxygen from the flow channels to the catalyst. It is responsible for intensely damaging the cell's performance while in high current density, which is required to deliver the high-power performance expected from the automotive sector. In the pursuit to comprehend what is its source, characterization of the components related to the mass transport were analyzed to quantify their contribution to the overall transport loss (Choo *et al.*, 2015; Srouji *et al.*, 2017; Williams *et al.*, 2004a; Williams *et al.*, 2004b).

Assuming a 1-dimension model basis, researchers have tried to fraction the loss into Fickian and non-Fickian resistance, so they could infer Fick's law to understand its behavior. As the oxygen is seldom fed in a pure stream, it was found that mixing oxygen with helium instead of the usual nitrogen could help reduce the transport losses (Beuscher, 2006; Rho *et al.*, 1994a; Rho *et al.*, 1994b). Also following the line of Fick's law, the understanding that oxygen concentration is wholly consumed when reaching the surface of the catalyst layer, the concept of limiting current was introduced to evaluate this loss (Daniel R Baker *et al.*, 2006; St-Pierre *et al.*, 2007; Williams *et al.*, 2004b). Assuming that the oxygen concentration at the catalyst surface is zero, this simplifies Fick's equation, which will only depend on the oxygen concentration in the inlet of the fuel cell and one could calculate the mass transport resistance by the current maximum achieved.

Focusing in the pressure dependency of the mass transport phenomena, variation of the pressure and quantifying its impact in the overall transport loss has also been tried (Daniel R. Baker *et al.*, 2009; Benziger *et al.*, 2011; Kudo *et al.*, 2016; Nonoyama *et al.*, 2011; Sakai *et al.*, 2009). It was found that it can be decomposed into pressure-dependent resistance and pressure-independent resistance. The latter is believed to be correlated to the porosity of the CL structure and the permeability of the oxygen through the ionomer and the CL agglomerates. However, this assumption has not been verified yet as researchers disagree on the dimensions and interference of the Nafion thin film formed around the CL (Choo *et al.*, 2015; Sambandam *et al.*, 2013).

Applying *in-situ* techniques such as electrochemical impedance spectroscopy (EIS) measurements for diagnosing the mass transport resistance has proven to be reliable and cost-effective (Mitzel *et al.*, 2020; O'hayre *et al.*, 2016; Reshetyenko *et al.*, 2014; Springer *et*

al., 1996; Yuan *et al.*, 2007). According to Ohm's law, when plotting the impedance spectrum, each electrical element will produce a characteristic curve. Therefore, correlating the PEMFC operation within an equivalent electric circuit (EEC) allows the interpretation of the spectra and quantification of the data. This method was applied herein and despite the successfulness of the results, an observed hold back of this technique was that it does not present direct results and relies much on interpretation.

The determination of parameters and conditions that isolate the mass transport resistance is pivotal to understanding this loss. Most of the pre-cited studies have assumed 1-dimension flow, notwithstanding that modeling it in 3-dimensions has proven to be significant to the analysis of the flow field design and reactant consumption (Subbaraman *et al.*, 2010). The advance of the analytical technologies and techniques will shed light on the actual incognitos of the mass transport resistance as there is still much to be comprehended.

3 Materials and methods

3.1 PEMFC

The polymer electrolyte membrane fuel cell (Figure 3) used throughout the present study is manufactured by balticFuelCells GmbH model qCf Quickconnect with 25 cm² of active electrode area. The cell was placed in matching the cellFIX (Figure 4) device, also manufactured by balticFuelCells GmbH, that enables even pressure distribution in the active area, ensuring the reproducibility of the tests.

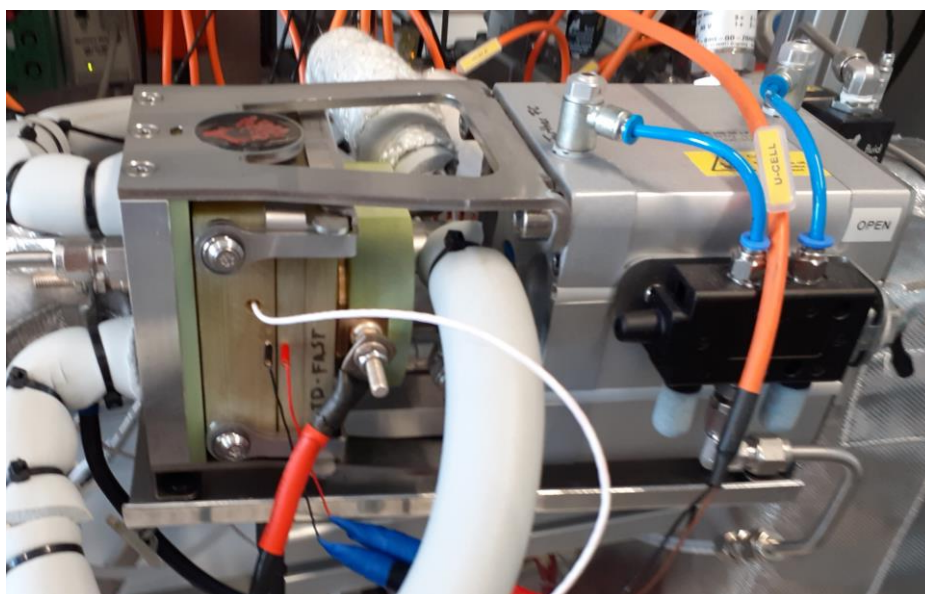


Figure 4 cellFIX device attached to the test station and with the PEMFC in place

The membrane electrode assembly (MEA) (Figure 5 A.1) used herein was a commercial MEA manufactured by Gore Fuel Cell Technologies with platinum loading of 0.1 mg/cm² in the anode side and 0.4 mg/cm² in the cathode side and membrane thickness of 18 μm. The desired size for the MEA was cut from the commercial sheet (5.5 cm x 5.5 cm even though the active contact area remained 25 cm²) and added in between the two GDLs inside the PEMFC for testing.

The gas diffusion layer (GDL) (Figure 5 A.2) was also a commercial product, Sigracet 25 BC from SGL Carbon GmbH with a total thickness of 235 μm and a treatment using 5 % Teflon. It was cut, and in the same fashion of the MEA, the desired size was cut (5 cm x 5 cm) to overlay both GCs. The gaskets around the GCs assured that once pressured, the fuel and the reactant would

not leak. Figure 5 B depicts the MEA, and the GDLs pressed together during routine maintenance.

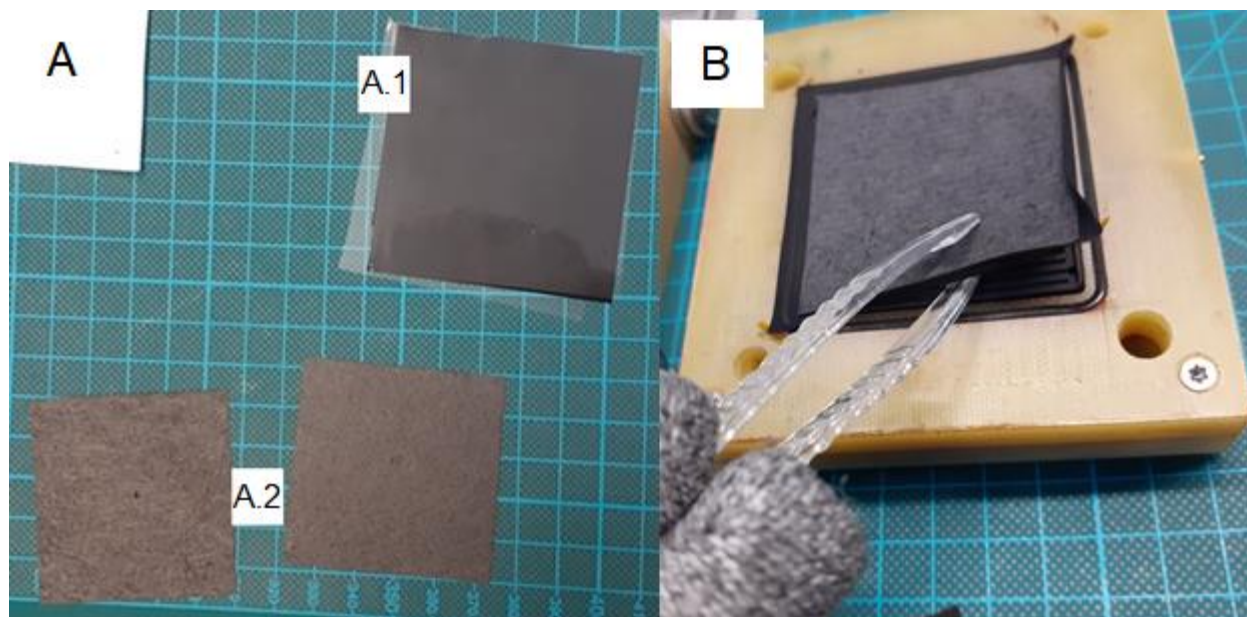


Figure 5 MEA (A.1) and both GDLs (A.2) cut from the commercial main piece. Assembled cell being maintained (B).

3.2 Performance test

The performance $j \times V$ (current density \times potential difference) tests were reproduced attaching the cellFIX device in the test station, an in-house product manufactured by DLR. It could control the fuel (hydrogen) and oxidant (pure oxygen, air, nitrogen) flow by different mass flow controllers calibrated with analogical signals to ensure precision. The gases passed through a bubbler before entering the cell to guarantee that the membrane was kept humidified during the measurements. The designated flow for each current density was calculated to avoid starvation issues, and it was maintained for 5 minutes to achieve performance stabilization and reliable data.

The load applied to the cell was maintained by a ZS electronic load (Figure 6) manufactured by Höcherl & Hackl externally connected to the cell with a maximum capacity of 60 A.



Figure 6 external ZS electronic load used on potentiostic mode

The cell was run at 80°C with anode and cathode feed streams humidified by the passage through the bubbler, in which temperature was also set at 80°C to ensure 100 % relative humidity of the gases. Consequently, the membrane is highly humidified and the impact of the ohmic resistance is minimized. The cell's gas inlets were kept at 85°C to guarantee that water would not condensate before entering the cell. The test station controlled the temperature from both, bubblers, and the cell's inlet, by electrical heaters. The cell temperature was maintained by an external circulator manufactured by Huber Kältemaschinenbau AG model Ministat 230.

Table 1 contains all the operation parameters for the polarization curves. The anode was kept in over stoichiometric flow to avoid any kind of resistance or interference in the measurement of the mass transport resistance in the cathode side. The highlighted parameters were the ones modified in the present study to assess their impact on performance and will be covered in more detail in sections 4.1 to 4.3. All the other ones are standard parameters validated by the automotive sector to assure the high performance of the fuel cell. This measurement aimed to compare the difference in performance when changing the stoichiometry and the oxygen concentration in the reactant stream and to qualitative assess the mass transport resistance region.

Table 1 Parameters applied to the PEMFC operation while running the tests

Parameter	Value
Cell temperature [°C]	80
Gas composition anode / cathode	100 % H ₂ / 10-100 % O ₂ in N ₂
Pressure anode / cathode [bar _{abs}]	2.2 / 2.0 and 1.5 / 1.5
RH anode / cathode [%]	100 / 100
Gas inlet temperature anode / cathode [°C]	85 / 85
Stoichiometry anode / Stoichiometry cathode[-]	2.0 / 1.6 - 2.2
Min. gas flow according to current density [A·cm ²]	0.2

3.3 Mass transport diagnosis

The interpretation and diagnosis of the performance curves were made with EIS measurements. This technique applies an excitation signal and records the system response to it. In this study, all the measures ran under galvanostatic mode, so the voltage changes accordingly to the

current chosen. The Nyquist plot was chosen to plot the impedance spectra as it has the imaginary part of the impedance plotted on the Y-axis and the real part on the X-axis. It depicts the impedance as a vector, and its shapes translate electrical elements. One shortcoming of this type of plot is not knowing in which exact frequency each data was recorded.

Typically, the impedance spectra for cathode resistances (due to the operating conditions, anode's resistances are minimal) include two semi-circles, one at high-frequency region and the other at low-frequency region. The first reflects the losses due to charge transfer or polarization resistances. The second arc, in the low-frequency region, is the subject of interest of this study as it depicts the resistance caused by transport resistance. This part will be covered in more detail in section 4.2.

The cell was connected to an external potentiostat/galvanostat, manufactured by ZAHNER-Elektrik GmbH & CoKG model PP240. The EIS measurements were taken at four different current loads: 0.625 A or 0.025 A·cm² with an excitation signal of 50 mA; 12.5 A or 0.5 A·cm² with an excitation signal of 1 A; 25 A or 1.0 A·cm² with an excitation signal of 2 A; 35 A or 1.4 A·cm² with an excitation signal of 2 A. Spectra were obtained from 10 kHz to 0.1 Hz and data acquisition time took around 5 min.

The Zahner application was used to record the spectra data and fit it to the chosen equivalent electric circuit (EEC). The fitting process correlates the plotted data within the behavior of the EEC and thus quantitatively assessing the spectra. The program allows us to fix some parameters while leaving others to be extrapolated, as depicted in Figure 7 A. During the simulation, the overall fitting error could not be over 3 % to assure reliable data (Figure 7 B). Data acquisition and the regression process will be analyzed in more detail in section 4.3.

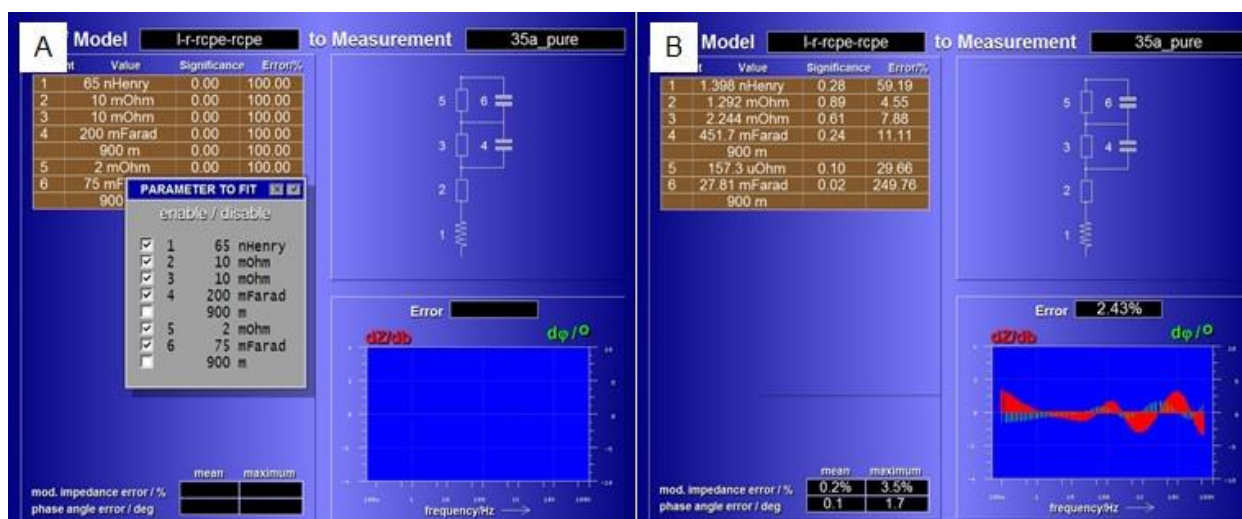


Figure 7 Display of the Zahner software to enable/disable parameters to customize the fitting (A). Results of the fitting (B)

4 Results and discussion

4.1 Polarization curves

The investigation of the impact on the cell's performance due to changes in stoichiometry and oxygen concentration can be visualized by plotting the potential measured in each current density. Each deflection observed can be correlated to a specific resistance or sum of resistances occurring inside the cell. Also, we can identify which operational conditions are more critical to the cell's overall efficiency.

Figure 8 demonstrates that increasing the oxygen concentration from 20.95 % (air operation) to 30 % (mix of air and pure O₂) does not induce a substantially better performance throughout all the different stoichiometry tested. However, lowering the oxygen concentration does negatively impact the performance, and the gap between the different oxygen concentrations get higher as the stoichiometry is lowered.

The characteristic drop in performance due to mass transport resistance is only slightly visible on high oxygen concentrations (above air operation) even on the lowest stoichiometry. The performance loss on those cases are more associated with ohmic and polarization resistances. Only a slight decay in Figure 8 A after 1.0 to 1.2 A·cm² is detectable, and this can be accounted to diffusion resistances. Actually, in Figure 8 C and Figure 8 D, a linear drop can be identified that strongly indicates ohmic loss due to ion transport resistance and, therefore, out of the scope of this study.

Figure 8 A and Figure 8 B is of particular interest, more precisely on the curves of 10 % and 15 % oxygen concentration because the nonlinear decay of mass transport resistance is very pronounced after 0.8 A·cm². Those curves represent the most critical operational conditions tested. Unfortunately, due to the limitation of the mass flow controllers installed on the test bench, it was not possible to measure above 1.2 A·cm² with 10 % oxygen concentration and respecting the preset conditions for avoiding starvation.

The first pronounced loss in performance at low current density, as determined by the Butler-Volmer equation, translates the activation overpotential. The parameter changes proposed in the study herein could only affect the exchange current density for the reaction (j_0) as it depends on both the concentration and the ratio of reactants and products. However, no significant variation could be detected, indicating that they all suffered from the same activation overpotential. This observation can be identified as the low current density region (0.0 A·cm² to 0.2 A·cm²) is almost identical in all tests and thus unaffected by the changes of the stoichiometry and oxygen concentration.

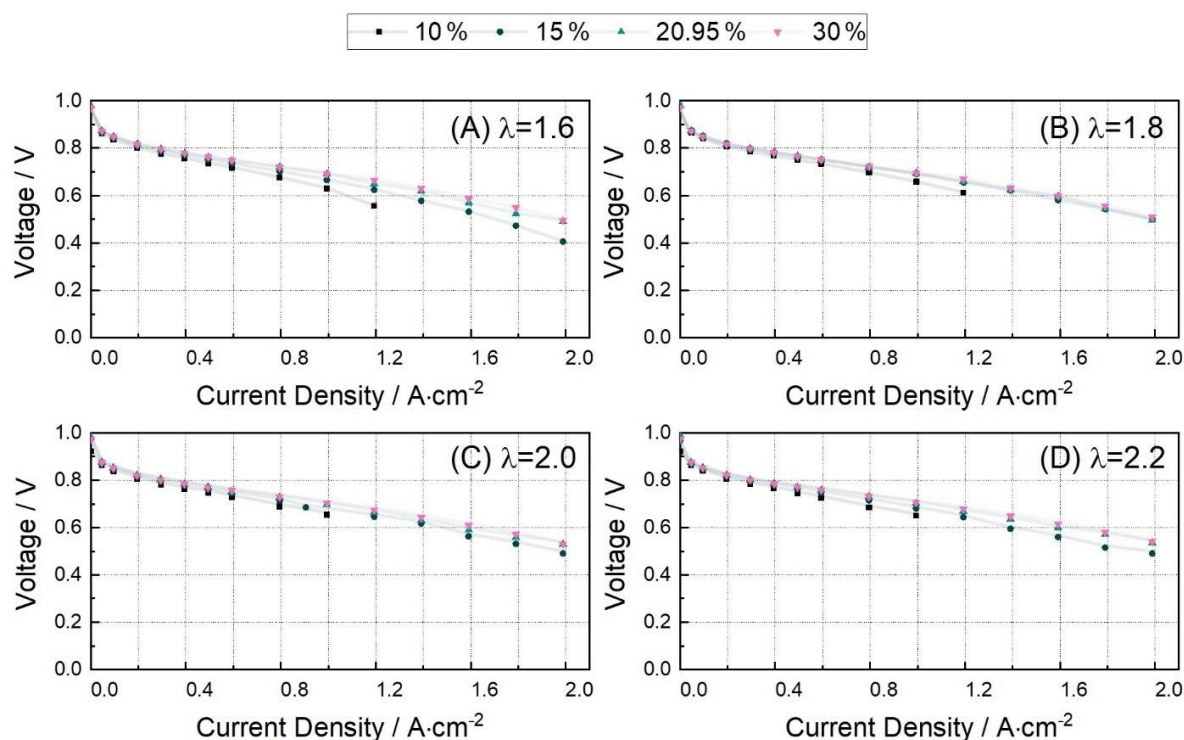


Figure 8 Impact of oxygen concentration change on the polarization curve plots grouped by stoichiometry (A) 1.6, (B) 1.8, (C) 2.0, (D) 2.2

In Figure 9, a closer look at the polarization curve with the stoichiometry of 1.6 is presented. A slight deviation from linearity starts to be noticed above $1.0 \text{ A}\cdot\text{cm}^{-2}$ for high oxygen concentrations (20.95 % and 30 %), while the characteristic nonlinear decay due to starvation is visually observed while operating with 15 % and 10 %. The impact of transport resistance on performance is exceptionally high on a 10 % measurement. Performance is drastically dropping within a short increase of current density. The mass transport phenomenon is definitely noticeable on 15 %, but its loss in performance is a bit smoother when compared with 10 %.

An additional measurement using pure oxygen with the same volume flow used on the 30 % oxygen measurement was done to determine the impact of the oxygen concentration on the performance of the cell. As disposed in Figure 9, the polarization curve obtained under pure oxygen condition does not show nonlinear performance loss at high current density, which accounts for mass transport limitations as predicted in Fick's law. The polarization resistance in the low current density region is the same as the other ones. Still, the open-circuit voltage (OCV) is slightly higher due to the higher oxygen concentration. Because the gas volume flow for the measurements using 30 % and 100 % of oxygen is the same and the amount of produced water is also the same, the water management inside the cell does not vary, and performance variations cannot be caused by changes in ohmic resistance due to different membrane humidification. The difference in the voltages between both measurements can only be referred to as mass transport limitations. Even if this limitation is only dominant at high current

density, its impact on the performance can also be detected at lower current density. The detectable diffusion resistance confirms this finding in this current density region in the EIS measurements presented in section 4.2.

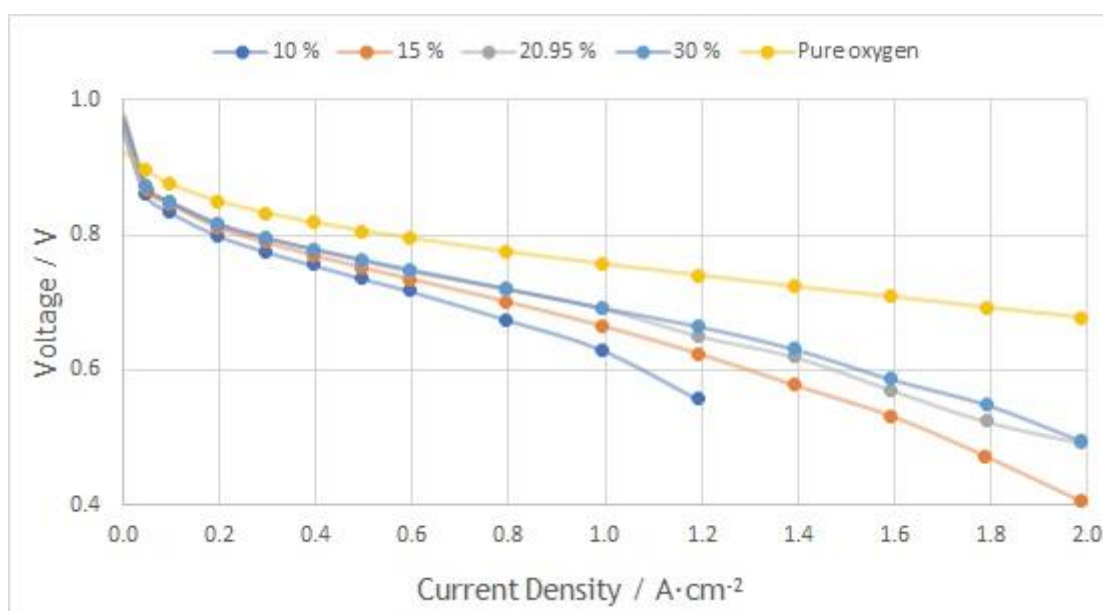


Figure 9 Closer look on the impact of oxygen concentration change for the polarization curve with stoichiometry of 1.6

Figure 10 shows a different perspective of the effect on the cell's performance by grouping the curves with the same oxygen concentration but varying the stoichiometry.

The stoichiometry factor appears to be a minor cause in performance loss as most of the curves overlay. Nevertheless, Figure 10 D shows a decrease in cell potential from the highest to lowest stoichiometry on the highest current density measured ($2.0 \text{ A}\cdot\text{cm}^2$). Thus, the most critical point of the curve is not substantial.

In Figure 10 C and D, it is possible to identify that the four different stoichiometry parameters tested actually converge into only two distinct patterns as the curves with the stoichiometry of 1.6 and 1.8 overlay, and so do the ones ran with the stoichiometry of 2.0 and 2.2. This leads to the interpretation that slight variations on stoichiometry coupled with high oxygen concentrations, do not impact the cell's performance. Also, the impact of stoichiometry can only be noticed when operating on $0.8 \text{ A}\cdot\text{cm}^2$ and above, the region dominated by mass transport limitations. Once again, the curves with 10 % and 15 % oxygen concentration coupled with the stoichiometry of 1.6 and 1.8 (Figure 8 A and Figure 8 B, respectively) can be used to present clear signs of mass transport resistance on high current density (above $0.8 \text{ A}\cdot\text{cm}^2$) and a nonlinear drop can be identified or more precisely the end of the linear decay.

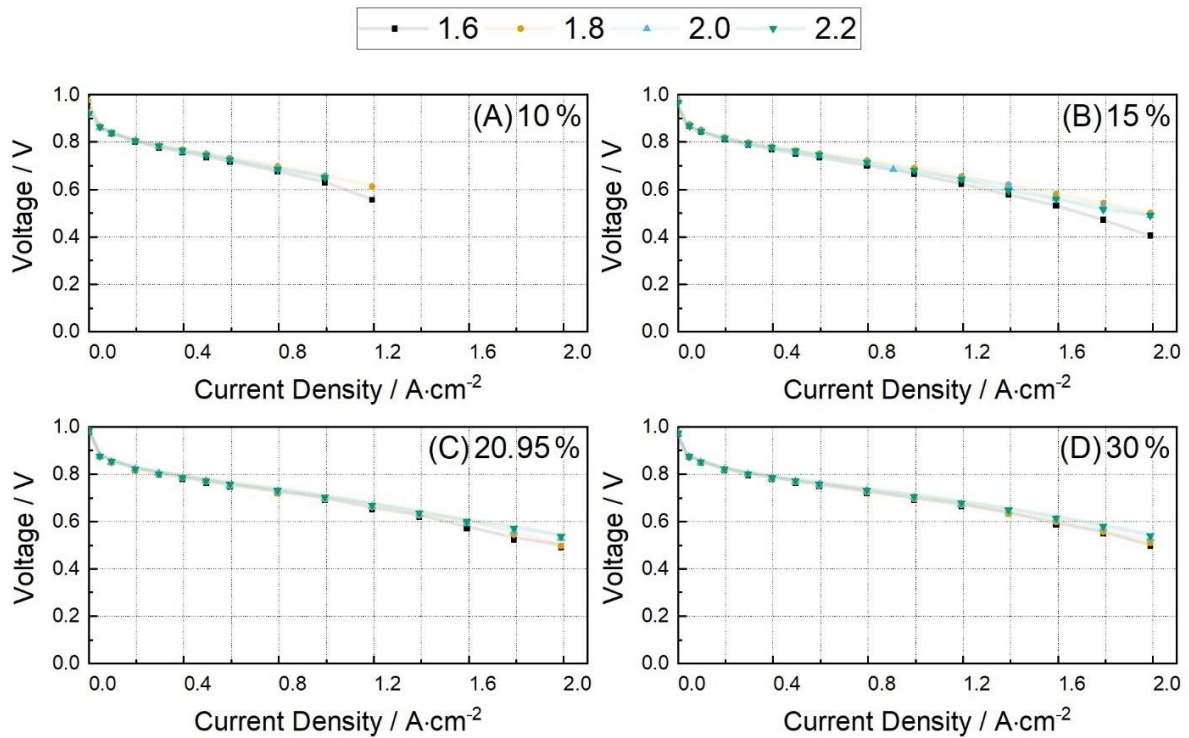


Figure 10 impact of stoichiometry change on the polarization curve plots grouped by oxygen concentration (A) 10 %, (B) 15 %, (C) 20.95 %, (D) 30 %

In the same way as Figure 9, Figure 11 has a closer look at stoichiometry impact with 15 % oxygen operation as the 10 % measurement could not be realized to the entire current density range. As already mentioned, the stoichiometry does not seem to be a significant factor affecting performance. Still, what differentiates then is the pronounced transport limitations

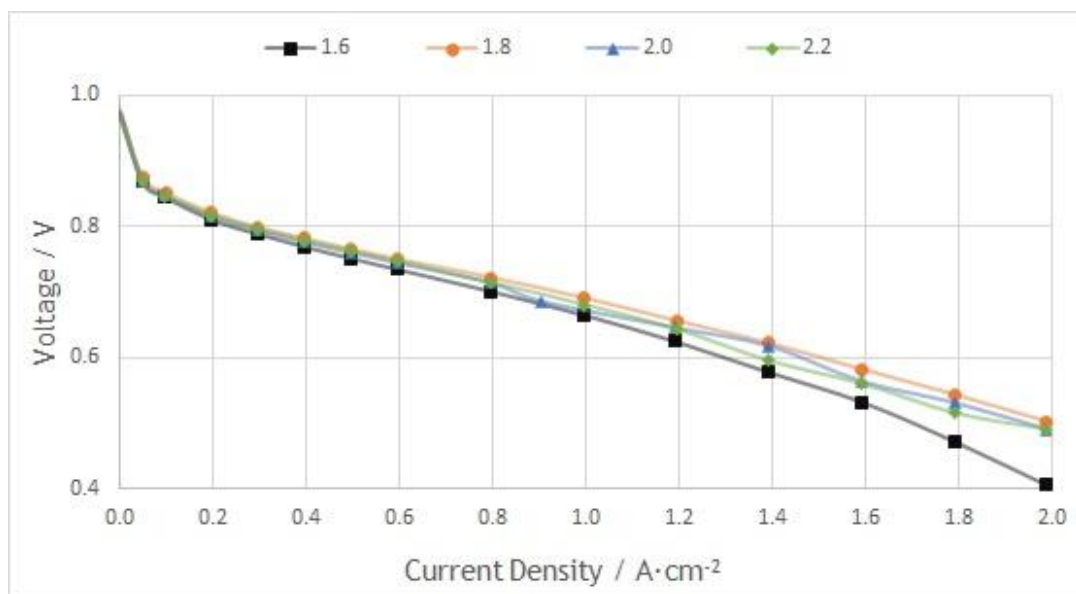


Figure 11 Zoom in of Figure 10 B - impact of stoichiometric change for the polarization curve with 15 % oxygen concentration.

observed when operating with an oxygen stoichiometry of 1.6, and its nonlinear decay is responsible for increasing the gap between this curve and the other ones.

The comparison of the polarization curve and the power attained gives better comprehension of the impact on performance. Figure 12 has plotted the four different oxygen concentration scenarios for stoichiometry of 1.6, considered as mentioned the most interesting for this study. Figure 12 B presents the only time that the maximum power was reached, meaning that going above $1.6 \text{ A}\cdot\text{cm}^2$ with those sets of parameters was not beneficial as more reactant and fuel were consumed, and less energy was delivered. This is correlated to the fact that it was not possible to identify the region dominated by mass transport resistance when operating with higher oxygen concentrations within the tested current density range. Therefore, there is some kind of plateau at about $1.0 \text{ W}/\text{cm}^2$ being reached in Figure 12 C and Figure 12 D close to $2.0 \text{ A}\cdot\text{cm}^2$ on the power curve couple with a slight tilt on the polarization curve, indicating that we may be entering the region dominated by mass transport resistance.

Even if Figure 12 A is not complete, the power curve is close to reaching its maximum by the current density of $1.2 \text{ A}\cdot\text{cm}^2$ as its derivative is almost getting to zero. It is interesting to stress that the power density maxima in Figure 12 A and in Figure 12 B are substantially lower compared to Figure 12 C and Figure 12 D. The power curve stops to linearly increase as the mass transport resistance the region is approaching. As temperature and relative humidity were the same, this must be caused by the lower concentration of oxygen that is sacrificing a considerable share of available potential to be able to produce electricity due to increased mass transport limitations. Namely, the diffusion of the oxygen through the nitrogen to the active catalyst surface is the rate-limiting step in this region.

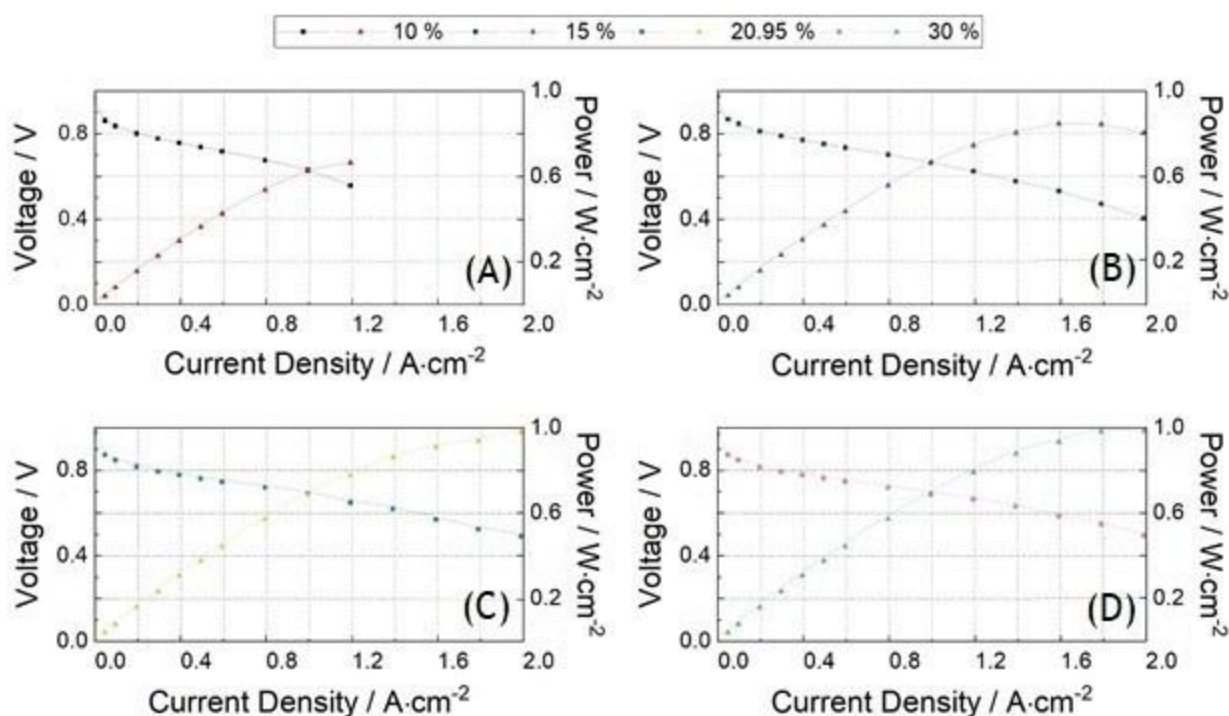


Figure 12 Comparison of the polarization curves and its respective power curve for the oxygen stoichiometry of interest (1.6) grouped by the different oxygen concentrations used

The quantification of the difference between performances, as shown in Table 2, can validate the observations made by inspecting the latest figures. At $0.5 \text{ A}\cdot\text{cm}^{-2}$, all the curves show the same trend of linear decay, and thus charge-transfer and ohmic resistance are dominating the performance loss. Ohmic resistance depends mostly on the membrane, temperature, and relative humidity and should be comparable in all experiments (mainly due to 100 % relative humidity of the feed gases). The EIS measurements confirm this fact in section 4.2. As discussed for Figure 8, the polarization resistance is mainly depending on the used catalyst and is also almost identical for all measurements. Consequently, the mass transport has only a slight impact in this region and operating at 30 % oxygen only induces a gain of 4 % in performance compared to 10 % oxygen concentration.

As mentioned previously, the measurements done with 10 % oxygen suffer from mass transport resistance as soon as the current density of $0.8 \text{ A}\cdot\text{cm}^{-2}$ is reached. This phenomenon induces a rapid decay in the polarization curve within short increases in current density. The data confirm those observations as we notice an increase of 19 % in power output at $1.2 \text{ A}\cdot\text{cm}^{-2}$ comparing the results from 10 % to 30 % in oxygen concentration.

Due to the limitation of the available mass flow controllers, the power output at higher current density can only be compared between 15 % and 30 % of oxygen concentration. A 22 % increase in power output at $2.0 \text{ A}\cdot\text{cm}^{-2}$ can here be detected.

Table 2 Voltage and power data (oxygen stoichiometry of 1.6)

O ₂ / %	0.5 / A·cm ⁻²		O ₂ / %	1.2 / A·cm ⁻²		O ₂ / %	2.0 / A·cm ⁻²	
	U / V	P / W		U / V	P / W		U / V	P / W
10	0.736	0.363	10	0.557	0.664	10	-	
15	0.735	0.372	15	0.624	0.745	15	0.405	0.805
20.95	0.761	0.376	20.95	0.650	0.776	20.95	0.492	0.978
30	0.764	0.377	30	0.664	0.793	30	0.495	0.984

The comparison of the performance of the cell on lower pressure could additionally validate the observations done in this study. Still, as presented in Figure 13 and Figure 14, the polarization curves were not stable during the measurements. The required change to measure higher current densities with 10 % oxygen did not anticipate that the flow needed on low current density would be out of the precision range of the new equipment (roughly 10 % of its maximum value), as shown in Figure 13. It is also suspected that the lower pressure could not be enough to push the water out of the cell while decreasing the load and, therefore, dropping the demanded feed. This might have made the water to block the channels, thus reducing the available active sites to the reaction take place. Consequently, the fuel cell could not be supplied with a constant and reliable gas flow for this test, and the cell voltage was not stable, as shown in Figure 14. Such tests would require further adaption of the used test bench.

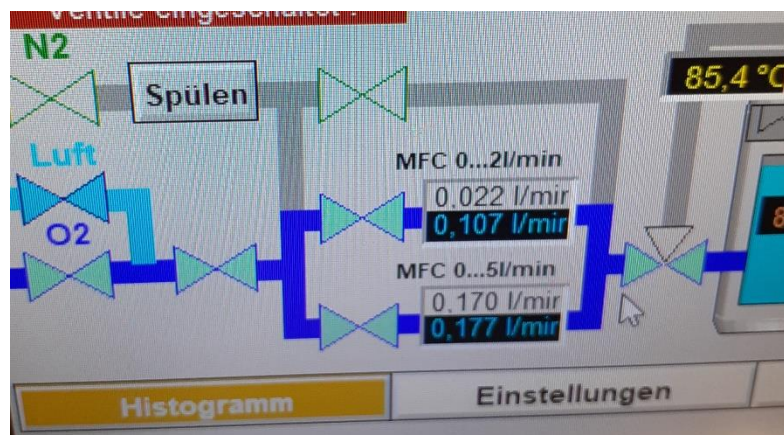


Figure 13 Instability of the flow meter for volumes under its precision range (roughly 10 % of its maximum value)

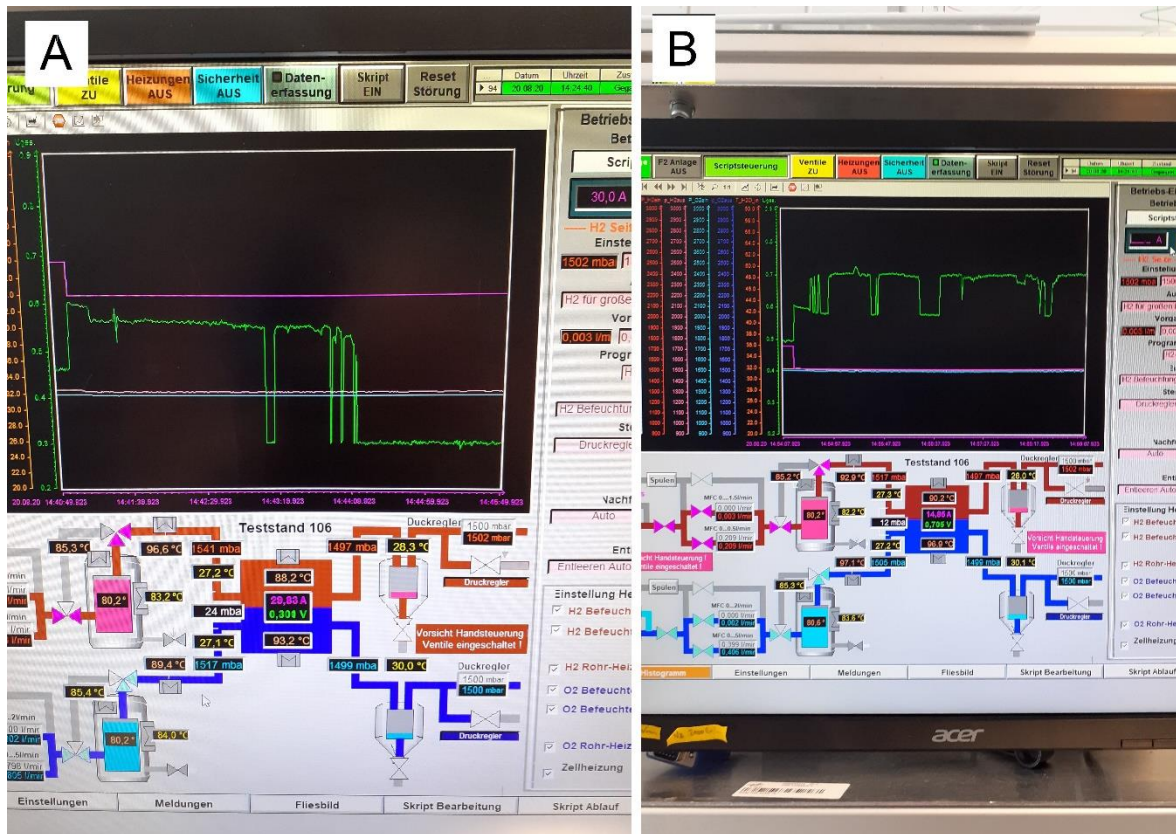


Figure 14 Test bench display while running the polarization curves with 1.5 bar and 1.2 A·cm⁻² (A) and 15 A (B). Sudden drops in performance were noticed and corrupted the data for making any precise analysis

4.2 EIS measurement

The measurements of impedance spectra can give first graphical indicators of the resistances in each specific current region drawn from the cell. The observed pattern in the Nyquist plot is characteristic of each type of resistance. The dominant resistance will overlay the other ones, or it is possible to identify different dominances in through the tested frequency range.

The cell was operated in galvanostatic mode, which means that a small sinusoidal current signal was super-positioned to the constant current drawn from the cell. The current values chosen for testing were 0.625 A (0.025 A·cm²), 12.5 A (0.5 A·cm²), 25 A (1.0 A·cm²), and 35 A (1.4 A·cm²), and the correspondent perturbations were of 50 mA, 1 A, 2 A and 2 A respectively. Due to restrictions on the gas mass flow controllers available, it was not possible to measure the EIS on 35 A and 10 % oxygen.

Figure 15 shows the EIS plots for all the tested currents with the oxygen stoichiometry of 1.6 on the different oxygen concentrations. It is possible to see the same pattern in all oxygen concentrations, only varying the size of each curve. The curve of 0.625 A is independent of the oxygen concentrations (also see Figure 16 A), while all the others reduce size as the oxygen

concentration is increased. This fact shows that the polarization resistance, dominant at this very low current density, is independent of the varied operating parameters and the significant impact on this resistance is the involved reactions to convert energy and the applied catalysts.

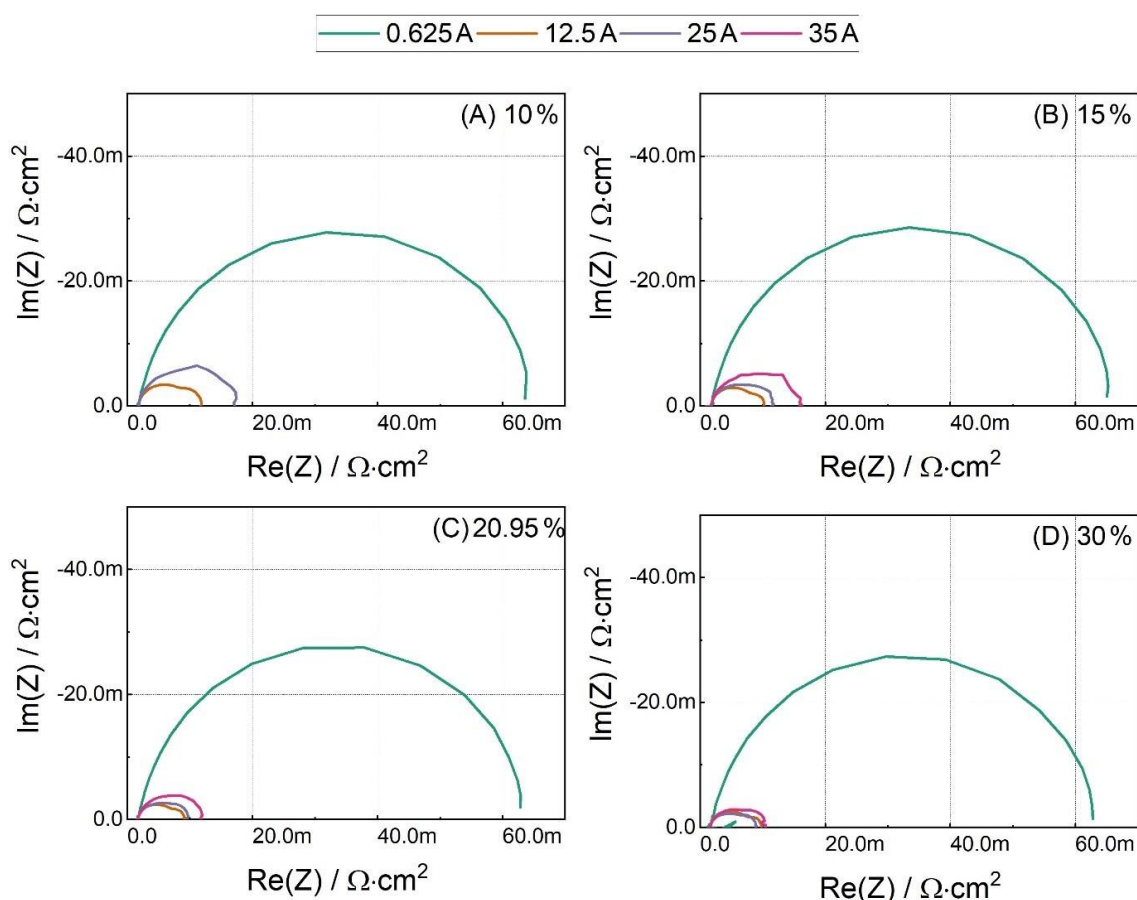


Figure 15 EIS plots for the stoichiometry of 1.6 (A) with 10 % oxygen, (B) with 15 % oxygen, (C) with 20.95 % oxygen, and (D) with 30 % oxygen

Figure 16 instead shows the plot for each load drawn and the impact of the variation of oxygen concentration on the reactant stream. From the polarization curves, there was no mass transport resistance region when operating with pure oxygen. This can be easily spotted in Figure 16 as it forms a perfect single semi-circle in all the currents tested and much smaller than all the other oxygen concentrations. Based on the spectra in Figure 16 A, only one non-ohmic resistance (one semi-circle) is available at a very low current density of $0.025 \text{ A}\cdot\text{cm}^2$. It is also clear that neither the ohmic resistance (x-axis cut at low $\text{Re}(Z)$) nor the polarization resistance (diameter of the semi-circle) is interfered from the oxygen concentration at this current density. This can lead to the same interpretation made to Figure 8 at low current density. However, operating at pure oxygen should decrease the activation overpotential as the difference in oxygen concentration is substantial, and thus, increasing the value of the exchange current density (j_0), which will reduce the activation overpotential as determined by the Butler-Volmer equation. However, the decrease in the activation overpotential when

operating with pure oxygen can be noticed at the low current density region in Figure 9. One must bear in mind that both analyses are complementary, and one does not invalidate the other. With increasing current density, a second overlapping semi-circle appears caused by mass transport resistance due to oxygen diffusion limitation. E.g., in Figure 16 C, the impact of the oxygen concentration is determinant, and operating with 10 % of oxygen is forming two semi-circles, which indicates the presence of this mass transport resistance.

Another important observation is that only in Figure 16 B shows that the mass transport resistance (second semi-circle) obtained while using 30 % oxygen was higher than 20.95 % of oxygen. This causes a crossing of the two spectra at low frequencies, an observation that can only be done in this current region. This highly exciting phenomenon will be addressed in more detail later as the impact of a different flow field design is evaluated.

It is also interesting to notice how the gaps between each oxygen concentration get more significant with the current increase. This can be correlated to polarization curves. As we go to higher current densities, they space themselves from each other. Based on the first visual evaluation, this seems to be caused by an increase of both non-ohmic resistance, charge transfer resistance (first semi-circle), and mass transport resistance (second semi-circle).

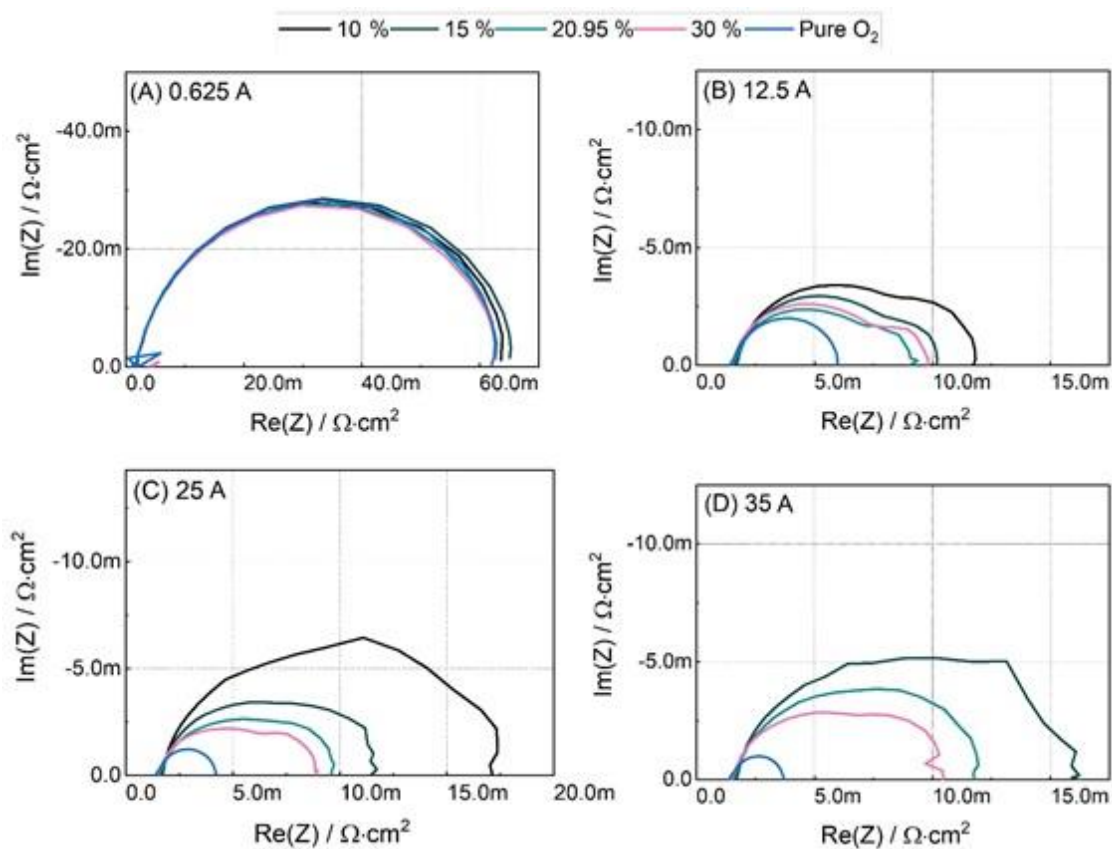


Figure 16 EIS plots for the stoichiometry of 1.6 measured with 0.625 A (A), 12.5 A (B), 25 A (C) and 35 A (D)

As already mentioned, the resistance observed at 0.625 A ($0.025 \text{ A}\cdot\text{cm}^2$) is due to polarization effects and are specific to the reaction employed on the energy conversion. Figure 17 exemplifies that there is no substantial distinction between the EIS plots throughout the oxygen concentrations used, and not even the stoichiometry had an impact on them. The measurements done under an operating pressure of 1.5 bar were added to Figure 17 to show that also the pressure is not impacting the resistance significantly in this region that is dominated by charge transfer only.

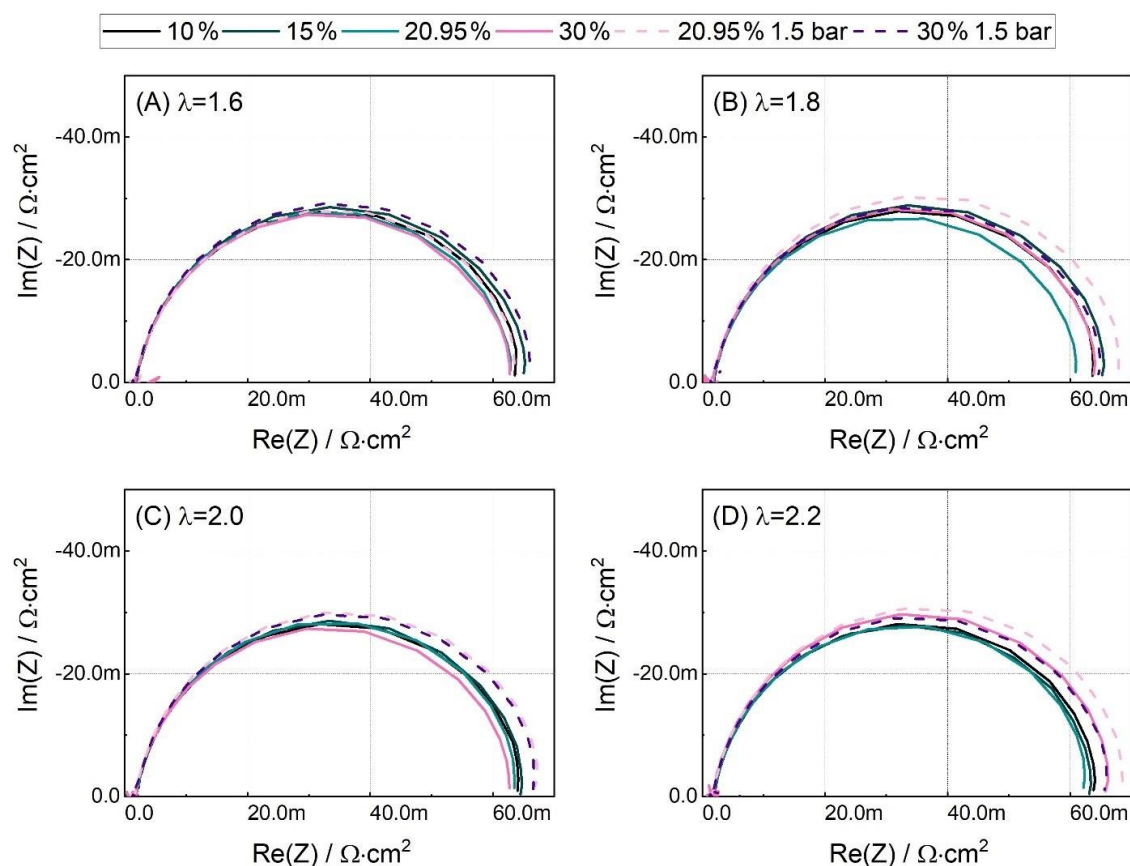


Figure 17 EIS plots for 0.625 A ($0.025 \text{ A}\cdot\text{cm}^2$) and a perturbation of 50mA under the oxygen stoichiometry of 1.6 (A), 1.8 (B), 2.0 (C), and 2.2 (D)

At $0.5 \text{ A}\cdot\text{cm}^2$ or 12.5 A from Figure 9, a difference or gap between the oxygen concentrations used becomes visible in the polarization curves. This trend is also reproduced in the EIS measurements. It is evident from Figure 18 that the increase in oxygen concentration reduces the resistance, and especially with 10 % oxygen, the resistance is significantly high. Comparing the shape of the 10 % curve in Figure 18 A and Figure 18 D makes it very clear to notice that changes in the transport resistance cause this difference. The two shaped semi-circle in Figure 18 A gives place to an oval shape in Fig 13 D, indicating that the transport resistance is reduced at higher oxygen stoichiometry.

Again, Figure 18 A and B present a fascinating situation as the 30 % curve is unexpectedly bigger than the 20.95 % one for the same stoichiometry. There is almost 10 % oxygen more in

the reactant stream, and it is suddenly affecting the cell's performance negatively while there is an evident trend of resistance reduction when there is more oxygen available. As already mentioned, this will be discussed more detailed during the validation of another flow field design.

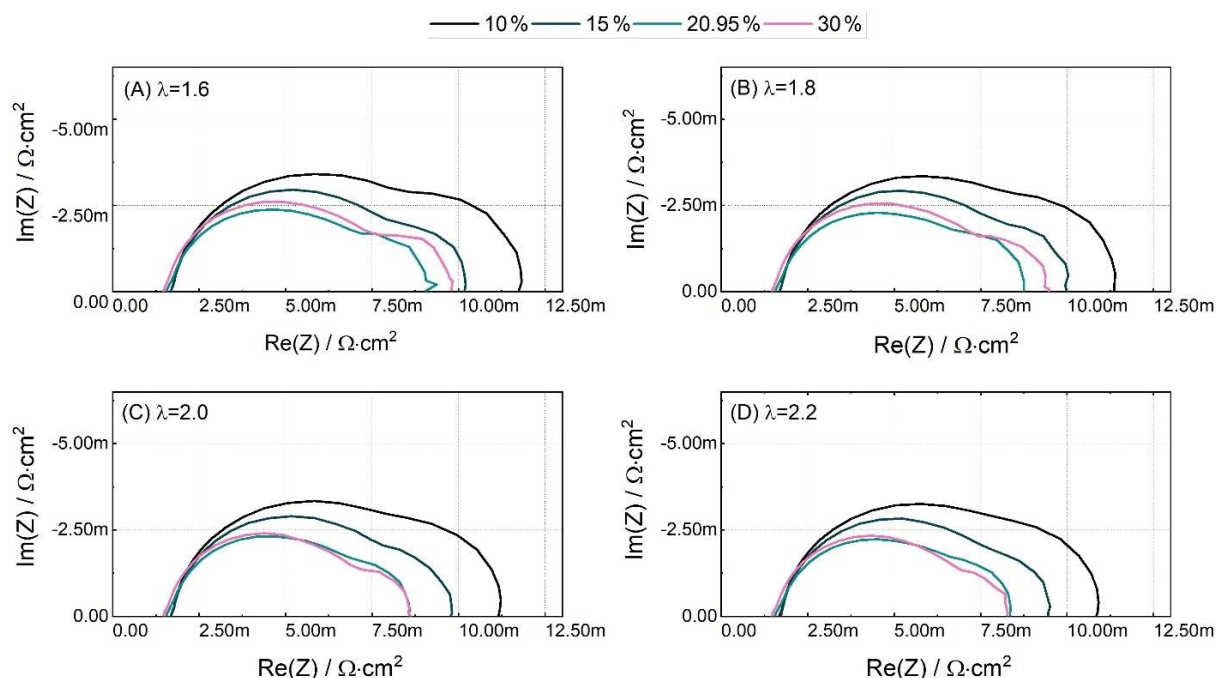


Figure 18 impact of the oxygen concentration on the EIS plots at 12.5 A ($0.5 \text{ A} \cdot \text{cm}^2$) for the oxygen stoichiometry of 1.6 (A), 1.8 (B), 2.0 (C), and 2.2 (D)

Changing the stoichiometry but keeping the same oxygen concentration has a lower impact on the performance as the other way around. That was noticed when comparing Figure 8 with Figure 10. The same trend is observed when making the same comparison but with the EIS plots. Figure 19 validates that. The most significant impact in resistance is when operating with 30 % oxygen. Generally, the effect on the first semi-circle (representing the charge transfer resistance) is minor.

In contrast, the impact on the second semi-circle is visible and follows the trend of lower transport resistance with higher stoichiometry. Additionally, the second semi-circle in these experiments is significantly smaller than the first one, indicating that the transport resistance is less dominant in this current density region. This can be correlated to the fact that the exponential drop in the polarization curve could not be detected at $0.5 \text{ A} \cdot \text{cm}^2$ when using lower oxygen stoichiometry.

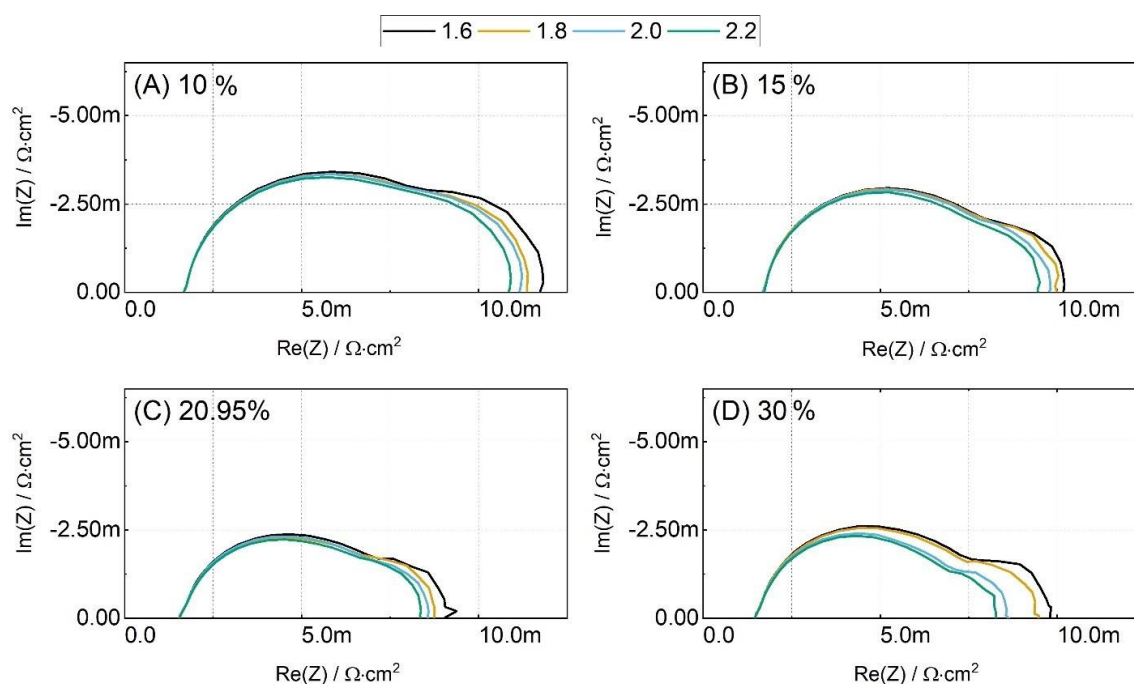


Figure 19 Impact of the oxygen stoichiometry change in the EIS plots measured at 12.5 A ($0.5 \text{ A}\cdot\text{cm}^2$) with (A) 10 % oxygen, (B) 15 % oxygen, (C) 20.95 % oxygen, and (D) 30 % oxygen in the reactant stream

Figure 20 brings a closer look at the impedance plots at 12.5 A ($0.5 \text{ A}\cdot\text{cm}^2$) with high oxygen concentration with both the 2.2/2.0 bar and the 1.5/1.5 bar pressure conditions tested. The unexpected more significant resistance with 30 % at 2.2/2.0 bar is suspected to be caused by the water management of the cell. The gas flow at 12.5 A is relatively low and might not be enough to remove the produced liquid water from the cell. While the amount of produced water is the same for 20.95 % and 30 % of oxygen, the total gas flow is even lower when feeding the cell with 30 % of oxygen. This is caused by the lower amount of nitrogen in the gas mixture, while the oxygen stoichiometry and amount are constant.

Operating with 1.5/1.5 bar does not show the same result. Here the cell behavior is as expected without water management issues. Higher oxygen concentration results in lower mass transfer resistance. This indicates that the unexpected behavior only appears under high-pressure conditions. Because water vapor tends to condensate and form more liquid water under higher pressure, this corroborates to the hypothesis that the observed phenomena must be caused by the accumulation of liquid water in the flow field. This seems to be caused by the flow field configuration of the used cell.

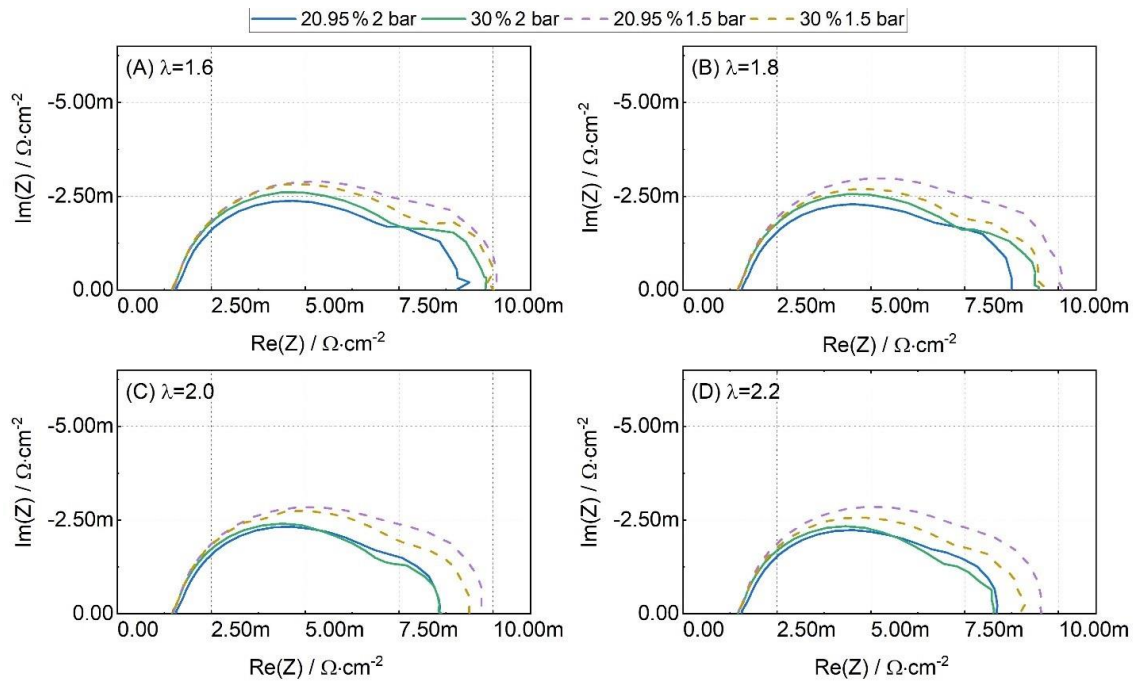


Figure 20 Closer look in the EIS plots at 12.5 A ($0.5 \text{ A}\cdot\text{cm}^2$) with different operating pressures and oxygen stoichiometry of (A) 1.6, (B) 1.8, (C) 2.0, and (D) 2.2

The commercial balticFuelCell single-cell setup used a particular multi-serpentine flow field and was employed at DLR in the European project ID-Fast. It consists of five parallel channels which are merged to one channel every time the flow direction is changed. Thereby, a serpentine flow across the active area, changing the flow direction four times, is realized, as shown in Figure 21 A. This hypothesis for the increased water accumulation is that each of the five parallel channels can be easily blocked by water. At the same time, the gas flow is maintained through the other channels. All channels are only required at high flow conditions. The blocked channels reduced the active area and increase the mass transport resistance for the oxygen due to the increased amount of liquid water in the cell.

An alternative single-serpentine flow field design (based on the European project Further FC) with only one channel was manufactured and tested to validate this hypothesis (Figure 21 B). Using only one single channel should avoid the accumulation of water in the flow field because there are no parallel channels for the gas available.

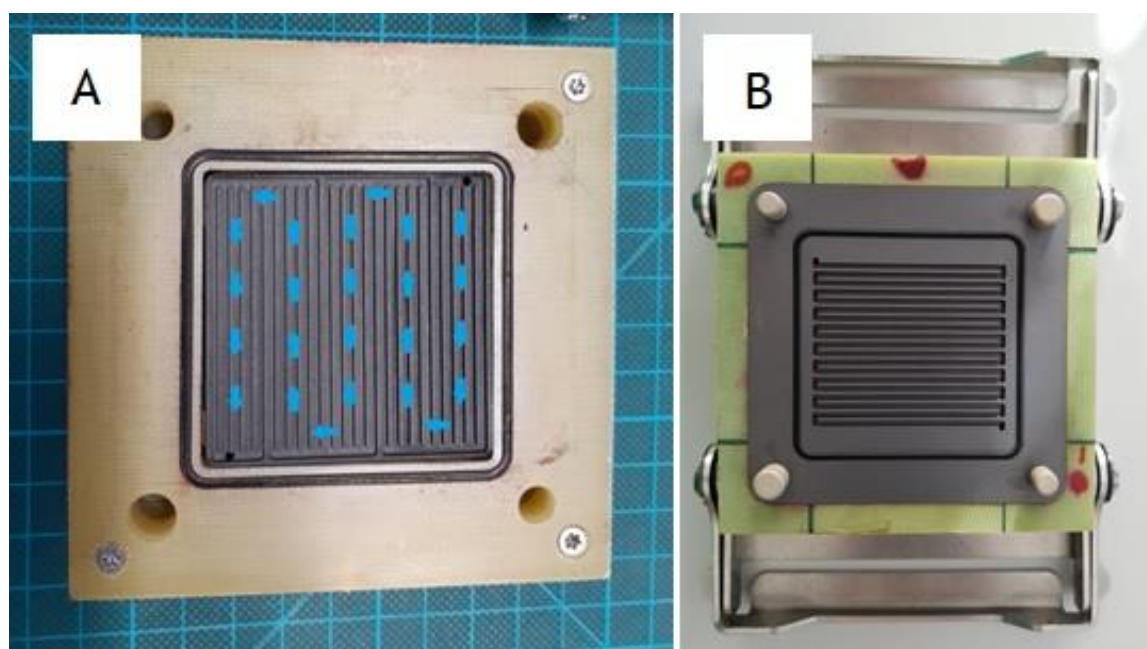


Figure 21 Flow field of the ID fast fuel cell (A). The blue arrows indicate the path followed from inlet to outlet. Single-serpentine flow field design tested (B)

Figure 22 confirms the assumption of water management issues on this current density as it compares the multi-serpentine flow field (ID-Fast) with the single-serpentine flow field (Further FC). The EIS plots for 30 % oxygen using the Further FC setup are smaller than the ones with 20.95 % oxygen in the same cell. There is no doubt then that unexpected, more significant resistance with 30 % oxygen was caused by the configuration of the flow field of the ID fast fuel cell. The higher total resistance of the Further FC setup is caused by the reduced active area of the cell.

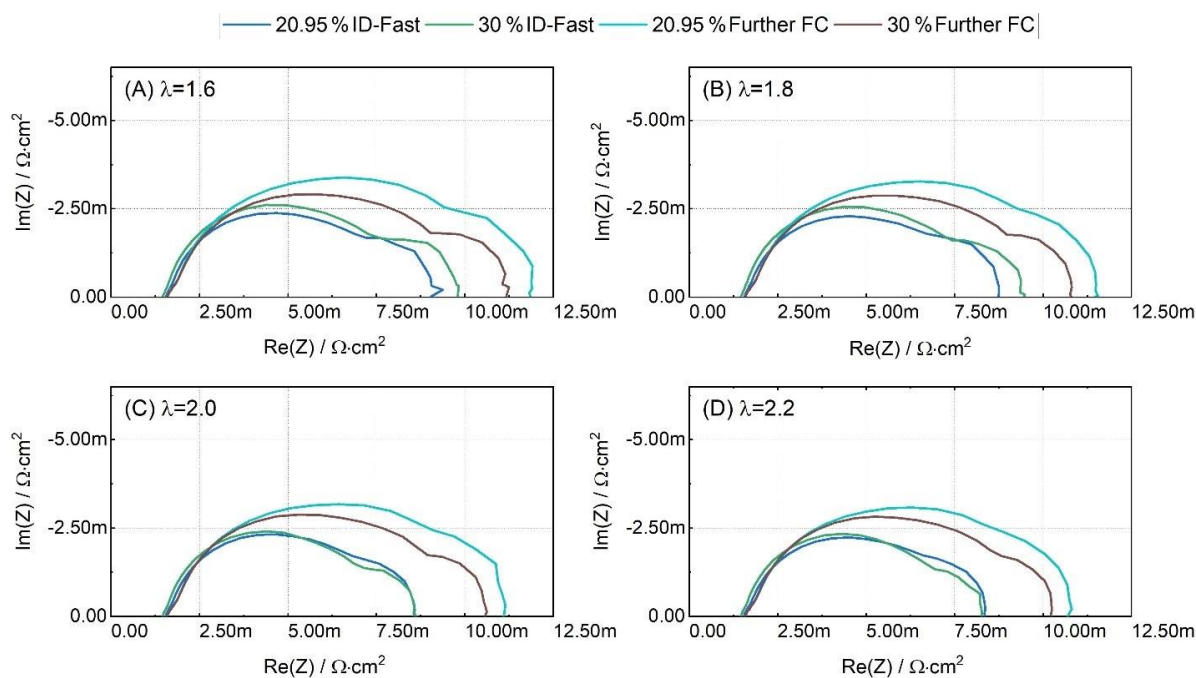


Figure 22 - Impact of the flow field structure on the EIS plots at 12.5 A ($0.5 \text{ A}\cdot\text{cm}^2$) at 2.2/2.0 bar with the stoichiometry of (A) 1.6, (B) 1.8, (C) 2.0, and (D) 2.2

The EIS plots at 25 A ($1.0 \text{ A}\cdot\text{cm}^2$) are shown in Figure 23, and the resistances follow the apparent trend of lower impedance with higher oxygen concentration. But the identification of the different resistances is difficult. At 30 % oxygen, the two semi-circles can be noticed while in the other concentrations, and they are bounded in an oval shape curve. Increasing the stoichiometry had a positive impact in the 10 % and 15 % oxygen curves, but almost unnoticeable when operating with the two highest oxygen concentrations.

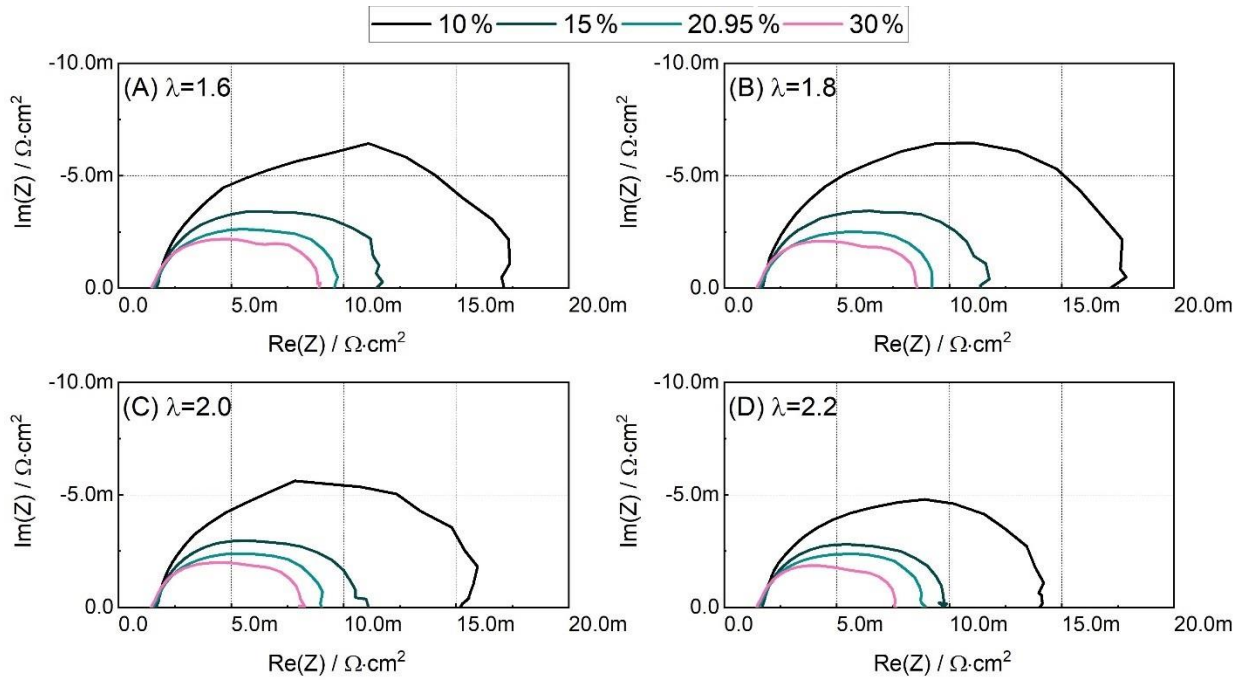


Figure 23 Impact of the oxygen concentration on the EIS plots at 25 A ($1 \text{ A}\cdot\text{cm}^2$) with the oxygen stoichiometry of (A) 1.6, (B) 1.8, (C) 2.0, and (D) 2.2

There is no obstruction on the flow field now as at 25 A, and the gas flow is high enough to remove the liquid water from the cell. The critical gas flow conditions for water accumulations seem to be limited to the low current density operation. Figure 24 shows the impedance plots for this current in a closer look with the same measurement but under low-pressure conditions. Only at 30 % oxygen and high stoichiometry of 2.2, the 1.5 bar's performance matches the one on standard operational requirements (air operation and 2.2/2.0 bar).

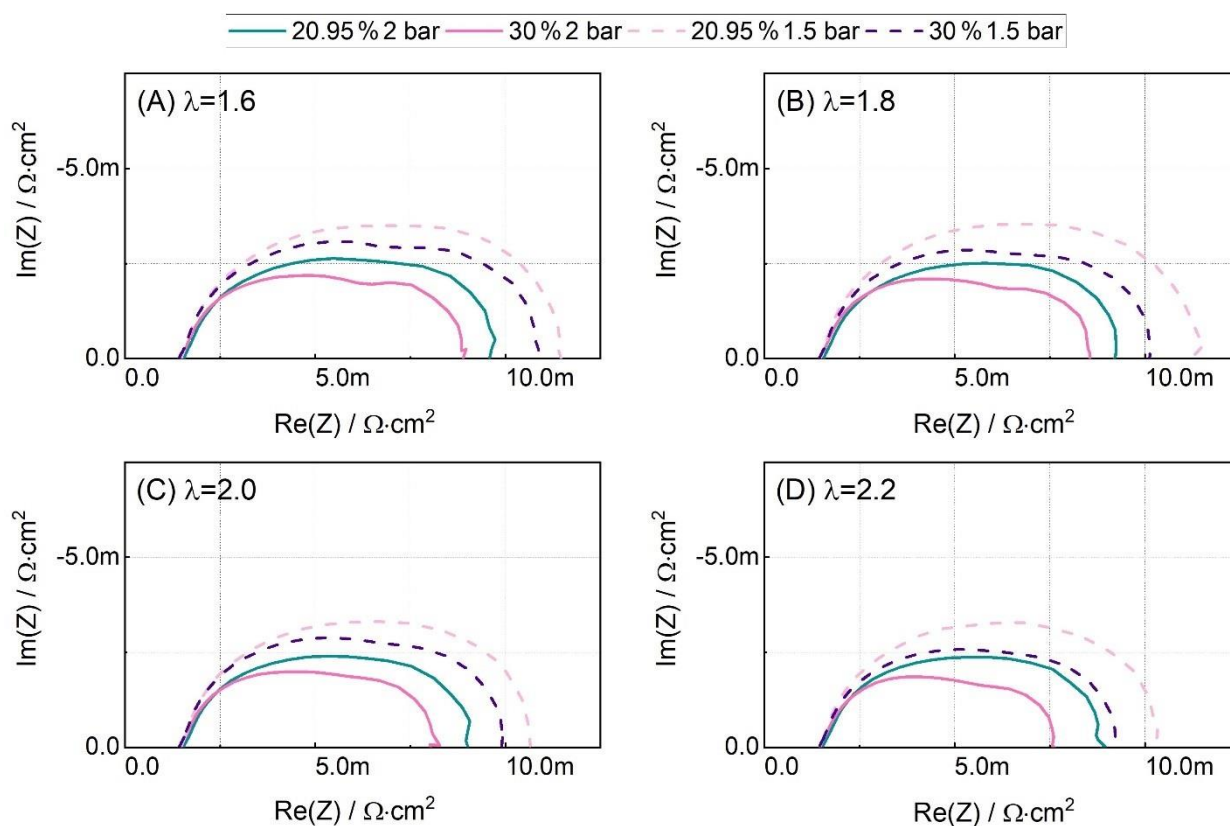


Figure 24 Closer look in the EIS plots at 25 A ($1.0 \text{ A}\cdot\text{cm}^2$) with different operating pressures and oxygen stoichiometry of (A) 1.6, (B) 1.8, (C) 2.0, and (D) 2.2

As was already mentioned, but due to the capacity limitations of the installed flow meters, it was not possible to reach 35 A, keeping the required amount of feed gases. For this reason, Figure 25 and Figure 26 start at 15 % oxygen.

At 35 A, all the EIS plots were positively affected by the increase in stoichiometry in an effective manner. This observation follows what has been seen in the polarization curves. The higher stoichiometry on high current density is responsible for diminishing the effect of mass transport limitations. Comparing Figure 25 A and Figure 25 D, it is also possible to visualize that at higher stoichiometry, the difference in the utilization of 20.95 % oxygen and 30 % oxygen is not substantial face the gap between them and the 15 % oxygen curve.

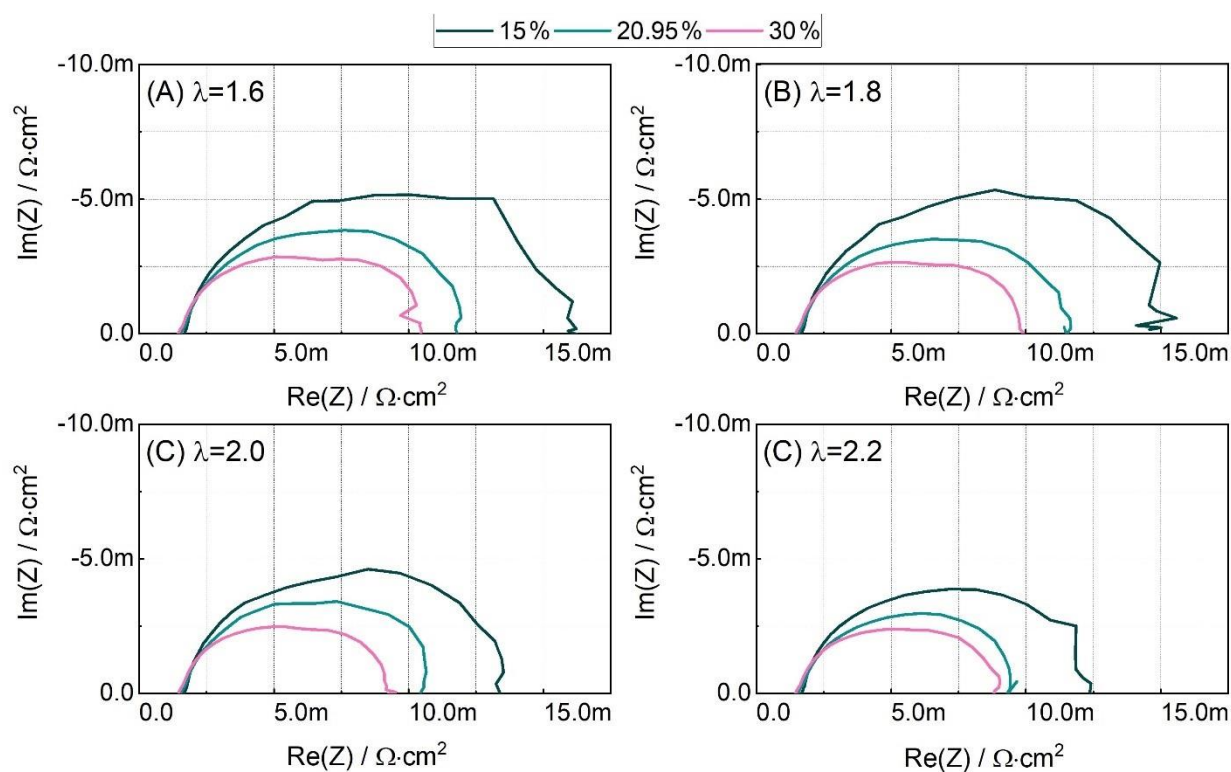


Figure 25 Impact of the oxygen concentration on the EIS plots at 35 A ($1.4 \text{ A}\cdot\text{cm}^2$) with the oxygen stoichiometry of (A) 1.6, (B) 1.8, (C) 2.0, and (D) 2.2

Figure 26 brings once again a closer look into the EIS plots with high oxygen concentration on the different pressures tested to analyze the impact of this parameter. In Figure 26 A, the curves start to get more space. The performance loss with air operation is positively affected by the pressure on high current density. The transport resistance is so substantial that the two semi-circles merge to form an almost perfect oval shape plot dominated by the mass transport resistance.

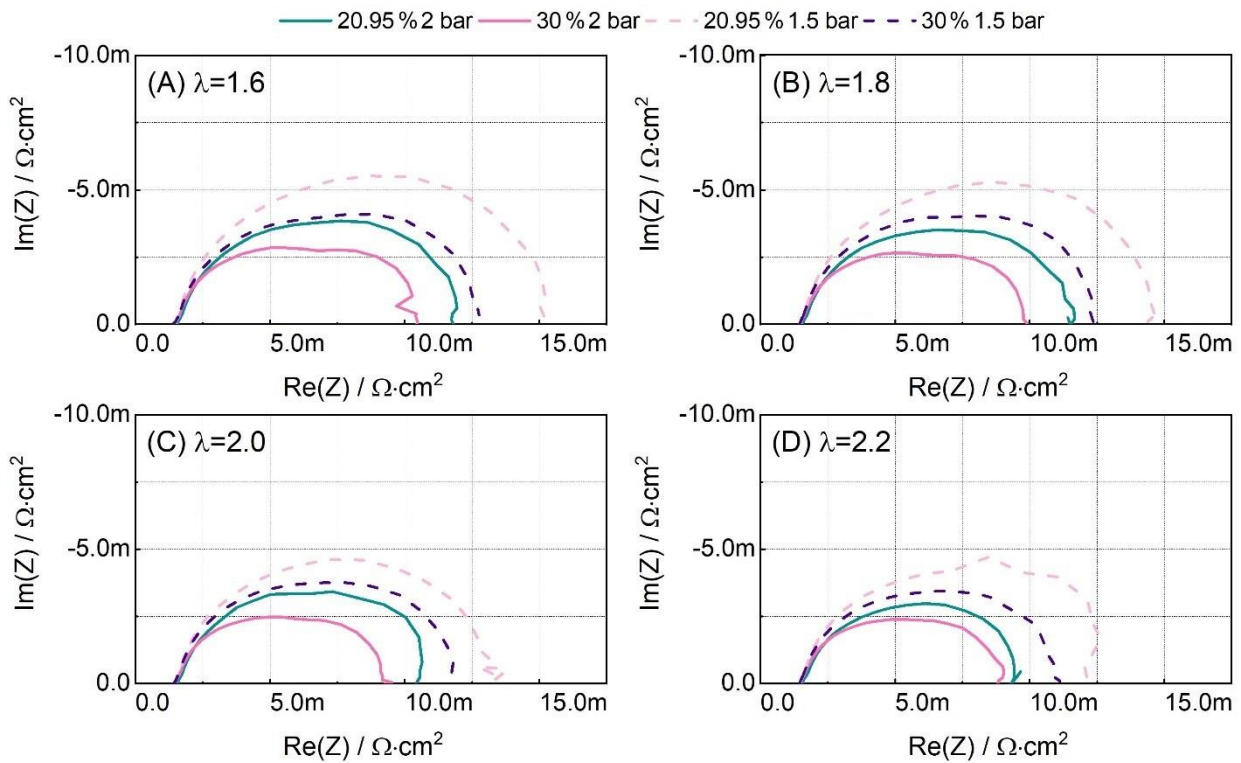


Figure 26 Closer look in the EIS plots at 35 A ($1.4 \text{ A}\cdot\text{cm}^2$) with different operating pressures and oxygen stoichiometry of (A) 1.6, (B) 1.8, (C) 2.0, and (D) 2.2

4.3 EIS fitting

Analyzing the EIS plots does not enable a quantitative assessment of the involved resistances. The fitting procedure tries to correlate the EIS plots with the EEC chosen to represent the behavior of the cell. The circuit chosen for the electrical characterization of this fuel cell is illustrated in Figure 27.

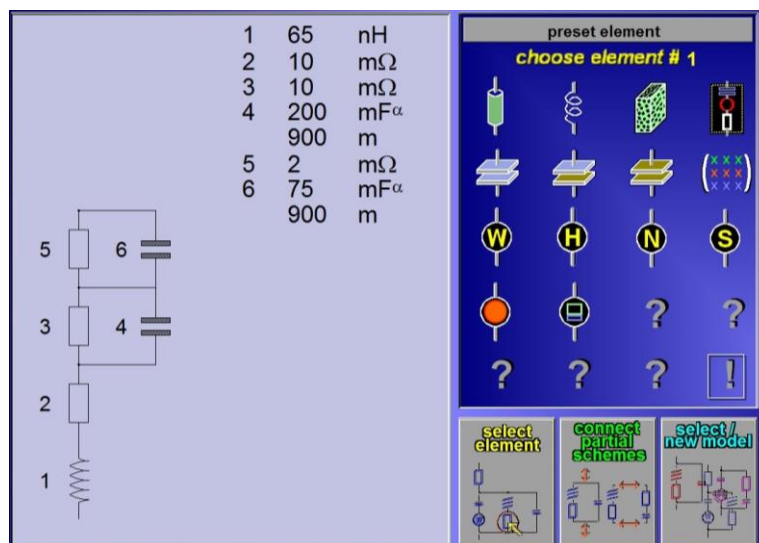


Figure 27 Zahner's display for modeling the electric circuit. The chose one has one inductive element (1), resistive element (2), and two parallel sets (RCPE) (3, 4, 5, and 6)

Modeling the EEC to match the performance of the cell is what will guarantee good fitting results and thus validate the model. As already mentioned, each electric element has a distinct response in the Nyquist plot. The closer the model's overall response is to the actual spectrum, the best. Figure 28 depicts a measured EIS spectrum overlaid by the response curve of the applied equivalent electric circuit..

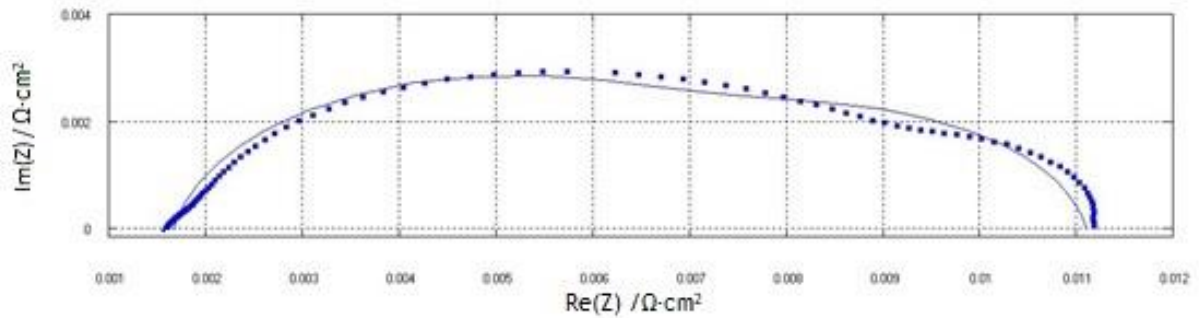


Figure 28 Comparison of the EIS spectrum (dotted line) and the model's electrical behavior plot (solid line)

The Zahner system has the Z-hit function that arranges the data collected and correlates it in curve so it can be manageable and fit the simulation (Figure 29). Once the data is then smoothed and the other parameters are selected (number of samples and the preferred interval), it is ready to simulate the impedance response of the electrical behavior of the cell.

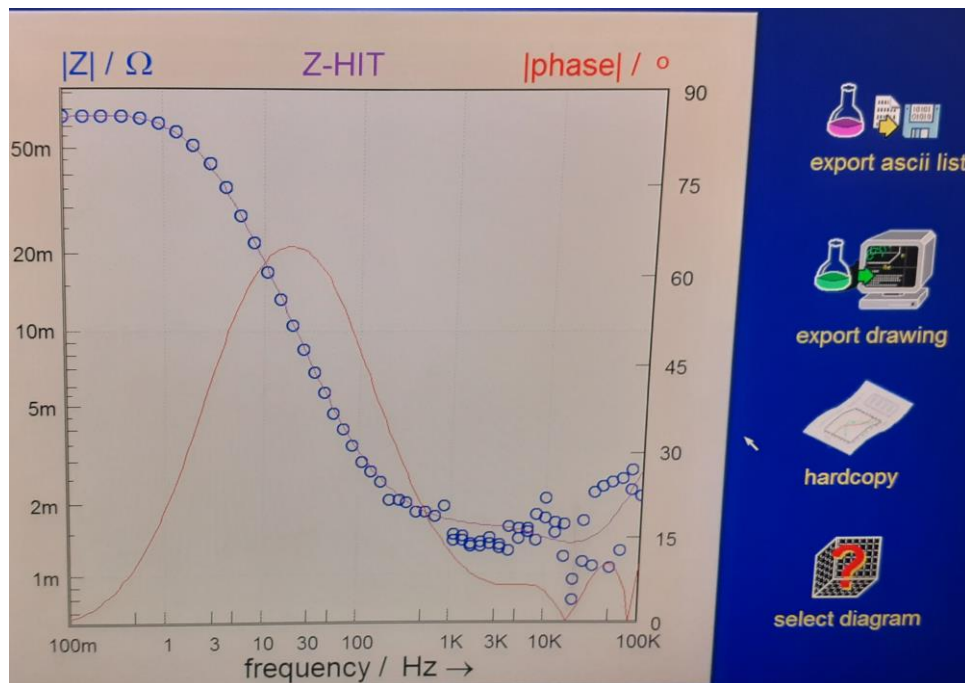


Figure 29 Z-Hit correlation done by the Zahner software to enable interpolation of the data in the fitting procedure

Figures 30 to 33 present the fitting results for the three different resistor elements present in the circuit. Each one of them is associated with a significant cause of resistance that affects

the cell's performance. R_{el} (ohmic or electrolyte resistance) and R_{pol} (charge transfer or polarization resistance) are out of the scope of this study and, therefore, will not have detailed interpretations. The focus of the research herein is the R_{diff} values as it translates the mass transport limitations.

Figure 30 represents the measurements taken 0.625 A or 0.025 A·cm². The diffusion resistance is not yet noticeable. R_{diff} is between 0.01 to 0.03 Ω·cm² and slightly inferior than R_{el} , which is around 0.02-0.05 Ω·cm². R_{pol} is by far the dominant resistance in the low current density region (LCD) with about 1.6 Ω·cm², a substantial difference of almost 100 times higher. It appears to be independent of air stoichiometry and oxygen concentration as the values seems to keep constant amid the changes in oxygen concentration and stoichiometry.

R_{el} demonstrates a slight trend of decreasing with low stoichiometry coupled with high oxygen concentration. Figure 30 B depicts R_{el} with the lowest values when measured with stoichiometry of 1.6 and 30 % oxygen in the reactant stream. This might be correlated to lower flow rates of gas entering the cell, and thus, more water is expelled, keeping the membrane more humidified.

Even if R_{diff} is not pronounced in the LCD, which validates the observations in sections 4.1 and 4.2, it is possible to notice a decrease in its value by the increase in the oxygen concentration of the feed stream and in the increase of the oxygen stoichiometry.

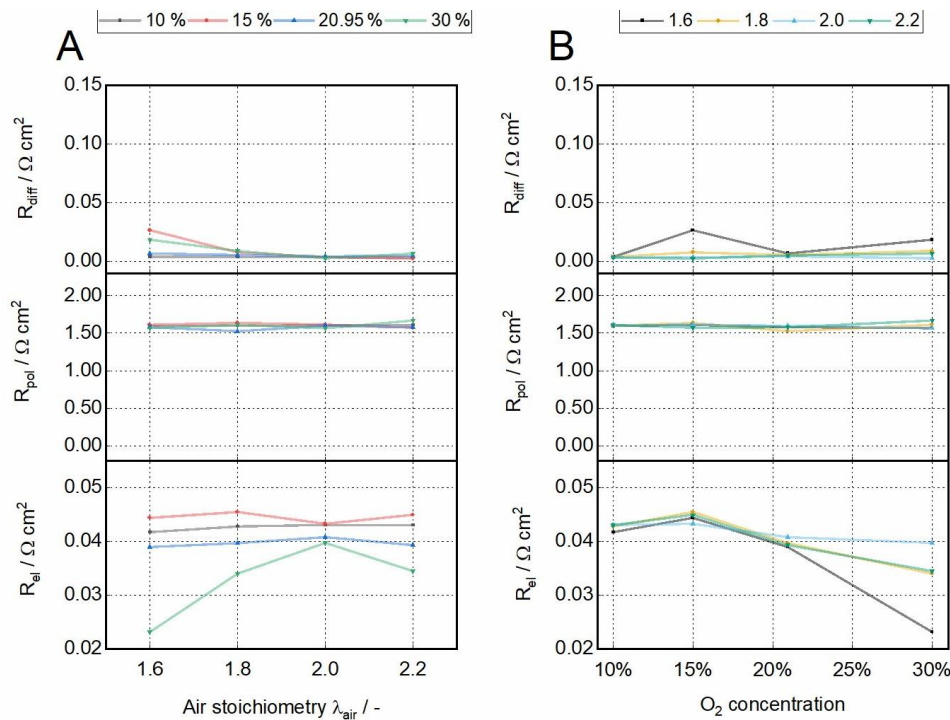


Figure 30 Fitting results for the EIS measurement of 0.625 A (0.025 A·cm²)

The situation changes completely as the cell current is increased (Figure 31). R_{diff} increases to values situated between 0.05 to 0.11 Ω·cm² and start to be comparable to R_{pol} values remain in

the same plateau but begin to be impacted by the changes in oxygen concentration and stoichiometry whereas with no clear trend or correlation to it. R_{diff} , on the other hand, shows to increase while the oxygen concentration is lowered. Stoichiometry does not seem to play much influence on it as curves in Figure 31 B practically overlay each other.

The flow field issue addressed in section 4.2 is not noticeable in the data assessed and thus cannot give a quantitative validation to assumptions made herein. Since R_{diff} and R_{pol} are in close value ranges, this might have misled the regression of the fitting procedure. However, this does not delegitimize the fitting process neither the conclusions made with Figure 22. As already mentioned, the fitting process will respond to the EEC model chosen, and this may indicate that it requires some adjustments to translate the cell's unusual behavior in this current density.

R_{el} remain in the same interval as in the previous assessment and is a minor resistance in the cell's overall performance. However, high concentrations of oxygen (and consequently low total gas flow) have a positive impact of slightly reducing this loss.

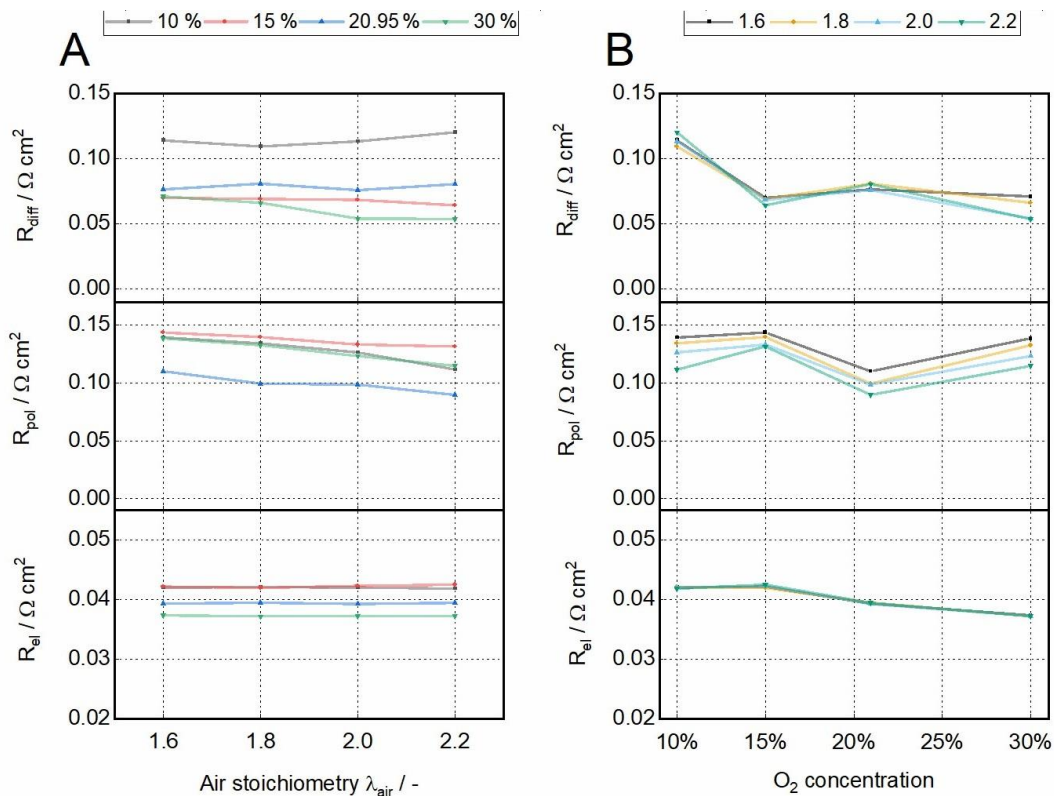


Figure 31 Fitting results for the EIS measurement of 12.5 A ($0.5 \text{ A} \cdot \text{cm}^2$)

Now at HDC (Figure 32), R_{diff} starts to dominate as it overcomes for the first time R_{pol} . R_{pol} also gets smaller (now from $0.05 \Omega \cdot \text{cm}^2$ to $0.11 \Omega \cdot \text{cm}^2$). R_{diff} is now on a range of 0.1 to $0.4 \Omega \cdot \text{cm}^2$. The mass transport losses are more than ten times higher when compared to the first values at low current density. Stoichiometry still not being relevant to the diffusion resistance as the oxygen concentration. The resistance with 10 % oxygen concentration is almost two to three

times higher than the other concentrations tested. This agrees with the polarization curves of Figure 9, which have shown a pronounced decay of the 10 % oxygen concentration curves just before the $0.8 \text{ A}\cdot\text{cm}^2$. In contrast, the others only developed a slight tilt.

The impact of the changing parameters in R_{pol} is still unclear. Values do not follow any specific pattern for changes in oxygen concentration neither to stoichiometry.

R_{el} values remain steady, around about $0.4 \text{ }\Omega\cdot\text{cm}^2$, and do not vary from $0.5 \text{ A}\cdot\text{cm}^2$ to $1.0 \text{ A}\cdot\text{cm}^2$ and showing the same trend as before.

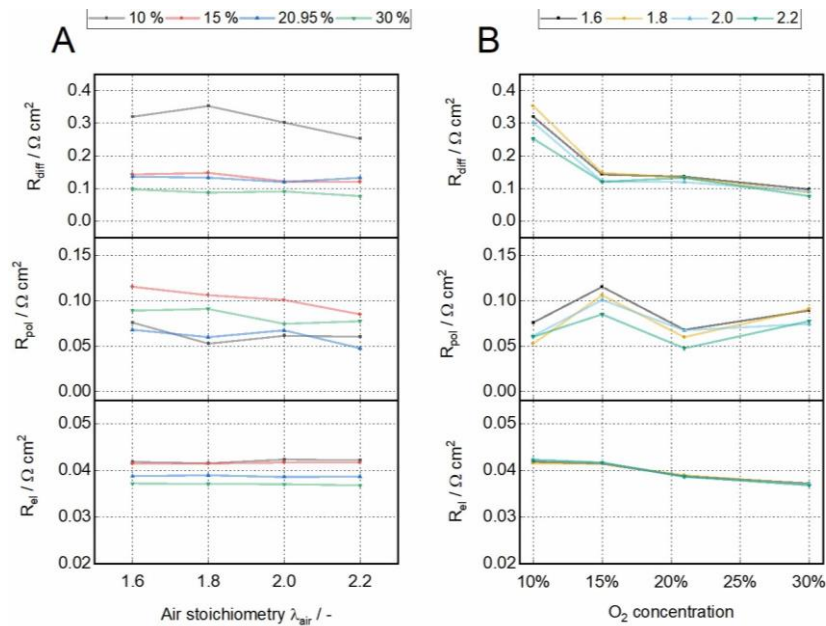


Figure 32 Fitting results for the EIS measurement of 25 A ($1.0 \text{ A}\cdot\text{cm}^2$)

At the highest current density assessed, $1.4 \text{ A}\cdot\text{cm}^2$, unfortunately, due to the limitations to the installed mass flow controllers and the available time frame for concluding this study, it was not possible to measure the impact of 10 % oxygen concentration in the feed stream (Figure 33).

Due to the fully humidified gases applied to the cell, R_{el} showed to be independent of the current density and parameters of interest and is almost constant during the entire study. Therefore, it correlates to the membrane material used only.

The values of R_{pol} decrease progressively as the current density increases. This might be caused by swelling of the membrane material in the catalyst layer. Due to Faraday's law, the further we go on HDC, the bigger the water production inside the cell, and thus the more humidified the catalyst layer gets. Consequently, the contact between the membrane material and the catalyst improves and the electrochemical active area of the catalyst could be increased, resulting in decreased resistances. The values still do not present any clear pattern to the changes in parameters and now range from 0.03 to $0.10 \text{ }\Omega\cdot\text{cm}^2$.

R_{diff} is substantially higher, now ranging from 0.1 to 0.3 $\Omega \cdot \text{cm}^2$ (and most likely significantly higher for 10 % oxygen concentration) and thus, the loss governing the cell's performance. There is a clear distinction between the diffusion resistances curves in Figure 33 A due to the oxygen concentration. Additionally, the 15 % oxygen concentration presented the highest decrease in resistance to the increase of stoichiometry. The impact by the stoichiometry for the other oxygen concentrations measured is only slightly pronounced. This validates the observations made in section 4.1 that the oxygen concentration was the primary factor affecting the cell's performance. Also, looking at Figure 33 B, one can see that the mass transport resistance curves decrease for all the plotted stoichiometry as the oxygen concentration on the X-axis increases. Comparing Figures 31 B to 33 B, it is noticeable that the slope regarding the positive impact of higher oxygen concentrations in the feed stream increases with increased current density.

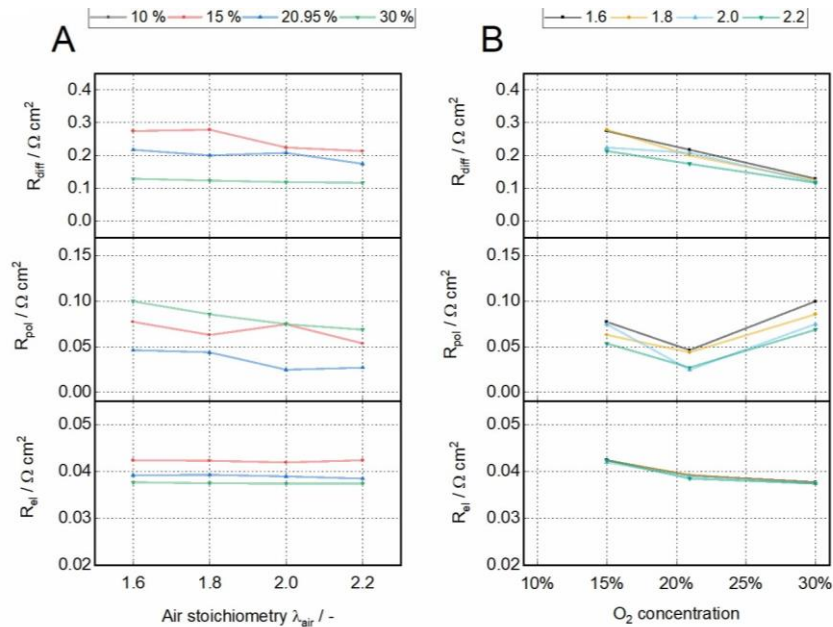


Figure 33 - Fitting results for the EIS measurement of 35 A ($1.4 \text{ A} \cdot \text{cm}^2$)

5 Conclusion

The present study aimed at to study the mass transport role on the energy conversion efficiency at PEMFC's cathode as a function of the oxygen concentration and stoichiometry. Plotting the current density (j) versus the delivered potential allowed assessing how the oxygen concentration correlates with R_{diff} . At the same time, the stoichiometry impact was not as noticeable. Fitting the Randle electrical equivalent circuit to the experimental impedance spectra, allowed to obtain the resistance parameters that characterize the PEMFC.

It was observed how the R_{diff} increases from a range of 0.01 to 0.03 $\Omega\cdot\text{cm}^2$ in LCD to 0.1 to 0.3 $\Omega\cdot\text{cm}^2$ in HCD and thus becoming the governing loss in the cell's performance. It increased by a factor of ten while R_{pol} decreased a few values, and R_{el} remained the same throughout the current density variations. This increase made the loss due to mass transport turn from the lowest value assessed in LCD to the highest in HCD. It reflects the most significant barrier for the high-power density desired by the automotive sector as the mass transport resistance is characterized by pronouncing an exponential decay in the performance curve. High mass transport limitations will translate into more unsatisfactory performance and shorter lifetime for the membrane and other components.

The higher humidification of the catalyst layer can explain the decrease in R_{pol} as the water production increase with the rise in current density. R_{el} and thus the membrane humidity was affected by the interchanging parameters.

The unexpected result of more significant total and mass-transport resistances with 30 % oxygen concentration than with air operation while taking the EIS measurements at 0.5 $\text{A}\cdot\text{cm}^2$ in both back pressures tested (2 bar and 1.5 bar) disagreed with the apparent observed trend of better performance with higher oxygen concentrations. This led to the hypothesis of poor water management inside the cell due to a multi-serpentine flow field configuration. A single serpentine flow was tested in the same conditions to confirm this assumption. The results showed which was expected by the hypothesis, more significant arcs in the spectra measured with 20.95 % oxygen concentration than in the ones with 30 % oxygen concentrations. Therefore, confirming that the multi serpentine flow field pattern struggled to expel the water produced in that current density. It might have been caused because the designed gas flow for this current density was not big enough to push all the water produced out of the cell, creating preferential paths, and thus reducing the active area for reaction. In higher current densities, it was not observed as the flows injected to the cell were considered high enough to purge the water produced out. However, it is significant to mention that even with the increased resistance at 0.5 $\text{A}\cdot\text{cm}^2$, the multi serpentine GC had better electrical performance. It produced

0.767 V and 0.758 V, air operation, and 30 % oxygen concentration, respectively, while the single serpentine GC had 0.736 V and 0.754 V, air operation, and 30 % oxygen concentration.

This occurrence can be highlighted as one of the most significant points of interest of the presented study as it demonstrates the efficiency of the in situ technique of electrochemical impedance spectroscopy for diagnosing the cell's operation without causing any kind of interference in the process. Furthermore, this study could overcome the issue of poor water management in medium current density operation by adapting of the flow field to a single-serpentine gas channel (GC). Consequently,, the characterization setup could be significantly improved for further research.

6 Assessment of the work done

6.1 Objectives Achieved

The present study's scope was to understand the transport limitations in the cathode of a PEMFC by interchanging two parameters in its feed stream, oxygen concentration and stoichiometry. It was possible to take enough measurements to assess the impact on the cell's performance to the variation of both parameters despite the limited time frame due to external conditions out of reach of action from the author and his supervisors (e.g., limited laboratory access during the Corona pandemic). The acquisition of the electrochemical impedance spectroscopy spectra allowed qualitative and quantitative diagnosis of the behavior of the internal resistances governing the cell's performance. It also validated the in-situ technique for inspecting for failures and abnormalities during operation as it was detected an issue of poor water management of the multi serpentine flow field pattern used. The main objectives of proposed by the study must be regarded as accomplished. Additionally, and not in the original scope of this work, the characterization setup used by DLR could be improved significantly for further research and the issue with the before used setup is now well understood.

6.2 Final Assessment

The author is delighted with the obtained results. The opportunity to him conceived to participate in this research has granted him academic skills and professional experiences that he will indeed use in his future. It has also been an extraordinary opportunity to put forth all the knowledge acquired throughout his university studies and acknowledge all the effort done by his teachers.

7 References

- Baker, D. R., Caulk, D. A., Neyerlin, K. C., & Murphy, M. W. (2009). Measurement of Oxygen Transport Resistance in PEM Fuel Cells by Limiting Current Methods. *Journal of The Electrochemical Society*, 156(9). doi:10.1149/1.3152226
- Baker, D. R., Wieser, C., Neyerlin, K. C., & Murphy, M. W. (2006). The use of limiting current to determine transport resistance in PEM fuel cells. *Ecs Transactions*, 3(1), 989.
- Benziger, J., Kimball, E., Mejia-Ariza, R., & Kevrekidis, I. (2011). Oxygen mass transport limitations at the cathode of polymer electrolyte membrane fuel cells. *AIChE Journal*, 57(9), 2505-2517. doi:10.1002/aic.12455
- Beuscher, U. (2006). Experimental Method to Determine the Mass Transport Resistance of a Polymer Electrolyte Fuel Cell. *Journal of The Electrochemical Society*, 153(9). doi:10.1149/1.2218760
- Biswas, I., Friedrich, K. A., Gazdzicki, P., Mitzel, J., & Schulze, M. (2020). Surface and Interface Science in Fuel Cell Research. *Surface and Interface Science: Volume 9: Applications I/Volume 10: Applications II*.
- Choo, M.-J., Oh, K.-H., Park, J.-K., & Kim, H.-T. (2015). Analysis of Oxygen Transport in Cathode Catalyst Layer of Low-Pt-Loaded Fuel Cells. *ChemElectroChem*, 2(3), 382-388. doi:10.1002/celec.201402354
- Fukuyama, Y., Shiomi, T., Kotaka, T., & Tabuchi, Y. (2014). The Impact of Platinum Reduction on Oxygen Transport in Proton Exchange Membrane Fuel Cells. *Electrochimica Acta*, 117, 367-378. doi:10.1016/j.electacta.2013.11.179
- Greszler, T. A., Caulk, D., & Sinha, P. (2012). The Impact of Platinum Loading on Oxygen Transport Resistance. *Journal of The Electrochemical Society*, 159(12), F831-F840. doi:10.1149/2.061212jes
- Handbook, F. C. (2004). Fuel Cell Handbook. In: US Department of Energy.
- Hogarth, W. H. J., & Benziger, J. B. (2006). Dynamics of Autohumidified PEM Fuel Cell Operation. *Journal of The Electrochemical Society*, 153(11). doi:10.1149/1.2344841
- Kabza, A. (2015). Fuel cell formulary. *Kabza, Ed*.
- Kongkanand, A., Gu, W., & Mathias, M. F. (2019). Proton-Exchange Membrane Fuel Cells with Low-Pt Content. In *Fuel Cells and Hydrogen Production* (pp. 323-342).
- Kongkanand, A., & Mathias, M. F. (2016). The Priority and Challenge of High-Power Performance of Low-Platinum Proton-Exchange Membrane Fuel Cells. *J Phys Chem Lett*, 7(7), 1127-1137. doi:10.1021/acs.jpcllett.6b00216
- Kudo, K., Jinnouchi, R., & Morimoto, Y. (2016). Humidity and Temperature Dependences of Oxygen Transport Resistance of Nafion Thin Film on Platinum Electrode. *Electrochimica Acta*, 209, 682-690. doi:10.1016/j.electacta.2016.04.023
- Larminie, J., Dicks, A., & McDonald, M. S. (2003). *Fuel cell systems explained* (Vol. 2): J. Wiley Chichester, UK.
- Mitzel, J., Sanchez-Monreal, J., Garcia-Sanchez, D., Gazdzicki, P., Schulze, M., Häußler, F., . . . Mielniczek, M. (2020). Fault Diagnostics in PEMFC Stacks by Evaluation of Local Performance and Cell Impedance Analysis. *Fuel Cells*.

- Nonoyama, N., Okazaki, S., Weber, A. Z., Ikogi, Y., & Yoshida, T. (2011). Analysis of Oxygen-Transport Diffusion Resistance in Proton-Exchange-Membrane Fuel Cells. *Journal of The Electrochemical Society*, 158(4). doi:10.1149/1.3546038
- O'Hayre, R., Cha, S.-W., Colella, W., & Prinz, F. B. (2016). *Fuel cell fundamentals*: John Wiley & Sons.
- Reshetenko, T. V., Bethune, K., Rubio, M. A., & Rocheleau, R. (2014). Study of low concentration CO poisoning of Pt anode in a proton exchange membrane fuel cell using spatial electrochemical impedance spectroscopy. *Journal of Power Sources*, 269, 344-362. doi:10.1016/j.jpowsour.2014.06.146
- Rho, Y. W., Srinivasan, S., & Kho, Y. T. (1994a). Mass Transport Phenomena in Proton Exchange Membrane Fuel Cells Using O₂/He, O₂/Ar, and O₂/N₂ Mixtures: II. Theoretical Analysis. *Journal of The Electrochemical Society*, 141(8), 2089.
- Rho, Y. W., Velev, O. A., Srinivasan, S., & Kho, Y. T. (1994b). Mass Transport Phenomena in Proton Exchange Membrane Fuel Cells Using O₂/He, O₂/Ar, and O₂/N₂ Mixtures: I. Experimental Analysis. *Journal of The Electrochemical Society*, 141(8), 2084.
- Sakai, K., Sato, K., Mashio, T., Ohma, A., Yamaguchi, K., & Shinohara, K. (2009). Analysis of reactant gas transport in catalyst layers; effect of Pt-loadings. *Ecs Transactions*, 25(1), 1193.
- Sambandam, S., Parrondo, J., & Ramani, V. (2013). Estimation of electrode ionomer oxygen permeability and ionomer-phase oxygen transport resistance in polymer electrolyte fuel cells. *Phys Chem Chem Phys*, 15(36), 14994-15002. doi:10.1039/c3cp51450 A
- Springer, T., Zawodzinski, T., Wilson, M., & Gottesfeld, S. (1996). Characterization of polymer electrolyte fuel cells using AC impedance spectroscopy. *Journal of The Electrochemical Society*, 143(2), 587.
- Srouji, A. K., Zheng, L. J., Dross, R., Aaron, D., & Mench, M. M. (2017). The role of water management on the oxygen transport resistance in polymer electrolyte fuel cell with ultra-low precious metal loading. *Journal of Power Sources*, 364, 92-100. doi:10.1016/j.jpowsour.2017.07.036
- St-Pierre, J., Wetton, B., Kim, G. S., & Promislow, K. (2007). Limiting Current Operation of Proton Exchange Membrane Fuel Cells. *Journal of The Electrochemical Society*, 154(2). doi:10.1149/1.2401045
- Subbaraman, R., Strmcnik, D., Paulikas, A. P., Stamenkovic, V. R., & Markovic, N. M. (2010). Oxygen Reduction Reaction at Three-Phase Interfaces. *ChemPhysChem*, 11(13), 2825-2833.
- Velders, G. J. M., Maas, R. J. M., Geilenkirchen, G. P., de Leeuw, F. A. A. M., Ligterink, N. E., Ruysenaars, P., . . . Wesseling, J. (2020). Effects of European emission reductions on air quality in the Netherlands and the associated health effects. *Atmospheric Environment*, 221. doi:10.1016/j.atmosenv.2019.117109
- Williams, M. V., Begg, E., Bonville, L., Kunz, H. R., & Fenton, J. M. (2004a). Characterization of Gas Diffusion Layers for PEMFC. *Journal of The Electrochemical Society*, 151(8). doi:10.1149/1.1764779
- Williams, M. V., Kunz, H. R., & Fenton, J. M. (2004b). Influence of Convection Through Gas-Diffusion Layers on Limiting Current in PEM FCs Using a Serpentine Flow Field. *Journal of The Electrochemical Society*, 151(10). doi:10.1149/1.1789791
- Wood, G., & Baker, K. (2019). *The Palgrave Handbook of Managing Fossil Fuels and Energy Transitions*: Springer.

Yuan, X., Wang, H., Colinsun, J., & Zhang, J. (2007). AC impedance technique in PEM fuel cell diagnosis—A review. *International Journal of Hydrogen Energy*, 32(17), 4365-4380. doi:10.1016/j.ijhydene.2007.05.036